Summer 11-2016

# Spatial Continuous Biomass Burning Emission Inventory: Application to WRF-Chem Model over the Northern Sub-Saharan African Region

Yun Yue
*University of Nebraska*, yunyue@huskers.unl.edu

# SPATIAL CONTINUOUS BIOMASS BURNING EMISSION INVENTORY: APPLICATION TO WRF-CHEM MODEL OVER THE NORTHERN SUB-SAHARAN AFRICAN REGION

by

Yun Yue

A THESIS

Presented to the Faculty of

The Graduate College at the University of Nebraska

In Partial Fulfillment of Requirements

For the Degree of Master of Science

Major: Earth and Atmospheric Sciences

Under the Supervision of Professor Jun Wang and Professor Qi (Steve) Hu

Lincoln, Nebraska

November, 2016

# SPATIAL CONTINUOUS BIOMASS BURNING EMISSION INVENTORY: APPLICATION TO WRF-CHEM MODEL OVER THE NORTHERN SUB-SAHARAN AFRICAN REGION

Yun Yue, M.S.

University of Nebraska, 2016

Advisors: Jun Wang, Qi (Steve) Hu

Fire, as a significant global source of trace gases and aerosol particles, plays an important role in perturbations of the chemical and physical properties of the atmosphere. Fire products from Moderate Resolution Imaging Spectroradiometer (MODIS) sensor on polar-orbiting satellites Terra and Aqua are largely used in several emission inventories. However, the MODIS fire products have inherent limitations due to the following reasons: (a) they cannot detect fires underneath clouds; (b) the fire detection sensitivity decreases at the edge of MODIS scan where viewing angles and MODIS pixel sizes are bigger than at nadir; and (c) there are gaps between MODIS swaths at the ground in low latitude regions. This study develops an empirical method to remedy these limitations and applied this method to improve pixel level emission, (hereafter the new emission). Another comparison emission, "scale old" emission, was also built after multiplying the daily domain emission ratio of new and original with original emission. In order to evaluate the bias correction method, three Weather Research and Forecasting model with Chemistry

(WRF-Chem) simulations were conducted using original (hereafter, old), new, and “scale old” emissions in January 2010 over the northern sub-Saharan African region. A two-day case study and assessment of the WRF-Chem simulation for one month show the new emission implementation improved the model performance especially at satellite gap and large viewing angle regions. The comparison between model simulated aerosol vertical profile and Cloud-Aerosol Lidar data with Orthogonal Polarization data also demonstrated the new emission increased the model performance.

# DEDICATION

This work is dedicated to my family and my friends who have always loved and supported me.

# ACKNOWLEDGEMENTS

First and foremost, I would like to sincerely thank my supervisor in the first three years of graduate study, Prof. Jun Wang, who has supported and led me to think and learn in a professional way. He and his research group have promoted and inspired me to improve myself to be better. His guidance helped me in all the time of finishing this thesis. I would also give special thanks to my current advisor Prof. Steve Hu for his patience, motivation, and immense knowledge. I would also like to express my sincere gratitude to Prof. Clinton Rowe for his ideas and comments to improve my thesis as my committee member.

I also thank the NASA Interactions and Feedbacks Between Biomass Burning and Water Cycle Dynamics Across the NSSA Region program led by Dr. Charles Ichoku for financial support for my thesis project. I appreciate the University of Nebraska-Lincoln Holland Computing Center for providing computing resources. I would also give special thanks to Yi Wang, Dr. Xiaoguang (Richard) Xu, and Thomas N. Polivka for their programming help and comments during my thesis writing. Lastly, I want to thank Darcy Pearcy for her selfless assistance to me in this thesis writing.

**Table of Contents**

# Chapter 1 Introduction

General public and scientific community's interests in emissions from biomass burning are growing because worldwide biomass burning contributes a large amount of greenhouse gases, trace gases such as carbon monoxide, nitric oxide, methane, and particulates into the atmosphere (Andreae 1991; Brass et al. 1996; Crutzen and Andreae 1990; Hao and Liu 1994; Heald et al. 2003; Ichoku and Ellison 2014; Shi et al. 2015). Gaseous and particulate emissions from biomass burning not only affect local air quality and landscape, but also can be transported by atmosphere for long distances to degrade visibility and air quality at downwind region (Wang et al. 2006), thereby altering the regional and global climate (Christopher et al. 1998; Crutzen and Andreae 1990). In addition to the direct effects of atmospheric physical and chemical properties and climate, biomass burning interacts with the biogeochemical, hydrological, and energy cycles on the Earth through a series of complex processes (Levine 1991). What is more, the increased levels of particulate concentration from biomass burning is believed to cause serious human health and public safety issues (Hyer et al. 2012; Lighty et al. 2000).

Most biomass burnings occur in the tropical regions (Brass et al. 1996; Hao and Liu 1994). In the tropics, fires are used for a variety of purposes: deforestation, shifting cultivation, fresh forage growth, agricultural residue clearing, and energy production for industrial and domestic use (Andreae 1991; Hao and Liu 1994; Ichoku and Ellison 2014). Over the past few decades, many studies have shown that biomass burning has raised $O_3$, CO, and other trace gases concentrations over the tropics (Andreae and Merlet 2001;

Andreae et al. 1988; Watson et al. 1990). Shi et al. (2015) evaluated the biomass burning emissions in three tropical regions (Central and South America, Africa, and South and Southeast Asia), and the results show that vegetation burning, fuelwood combustion, and human waste burning in 2010 contributed to 74% (530 Tg), 23% (170 Tg), and 3% (19Tg) of the total CO emissions in the three studied tropical regions, respectively. The three sources also accounted for 64% (4 Tg), 32% (2 Tg) and 3% (0.2 Tg) of the total Black Carbon (BC) emissions in the three regions (Shi et al. 2015). Their study indicates that Africa is the largest emitter among the three tropical regions.

As the largest continental source of biomass burning emissions (Roberts et al. 2009), biomass burning in Africa consumes millions of square kilometers of terrestrial vegetation every year, which account for 30% to 50% of the total amount of global vegetation burned each year (Ichoku and Ellison 2014; Roberts et al. 2009; Roberts and Wooster 2008). The released chemical components from the burning, as well as the emitted smoke aerosols into the atmosphere, modify the regional, and probably global, radiation energy balance of the Earth-atmosphere system (Andreae et al. 1998; Andreae and Merlet 2001; Ramanathan et al. 1985).

In order to accurately predict the tropical climate effects of biomass burning, to assess how fires change the socioeconomic landscape, and to reduce the uncertainties in describing such effects in atmospheric models, it is important to provide precise emission rates of biomass burning. Currently, because of the spatial and temporal varying nature of fires, the uncertainties in emission estimation remain large. In addition, *in situ* or ground-

based observations cannot provide reliable measurements of fire emissions globally (Ichoku et al. 2012; Roberts et al. 2009; Zhang et al. 2014). For this reason, satellite remote sensing is considered essential in evaluating smoke emissions and reducing the estimation uncertainties on regional-to-global scales by observing the active fire hotspots from space (Ichoku et al. 2012). Though geostationary satellites have received significant attention in generating the near-real-time emission inventory because of the relatively high frequencies to observe fire for a given region (Ichoku et al. 2012; Reid et al. 2009; Zhang et al. 2012), most of the global fire emission inventories rely on data from polar-orbiting satellite sensors such as Terra- and Aqua-Moderate Resolution Imaging Spectroradiometer (MODIS) (Darmenov and da Silva 2013; Ichoku et al. 2008; Kaiser et al. 2012; Wiedinmyer et al. 2011). However, on a single day, one MODIS sensor has only 16 pole-to-pole orbits, each producing a swath width of ~2300 km at the ground. Therefore, there remain significant gaps between MODIS consecutive ground tracks in the equatorial region (Freeborn et al. 2011). The fire detection sensitivity also decreases at the edge of MODIS scan where viewing angles and MODIS pixel sizes are bigger than at nadir.

These observational gaps and off-nadir detection limitations in MODIS fire products can result in absent and discontinuous information for emission estimation, leading to an underestimate of the total biomass burning emission. The emission estimate may also be biased to lower values because MODIS cannot detect fires under clouds. When this underestimated emission is applied to atmospheric transport and chemistry models, such as the Weather Research and Forecasting model with Chemistry (WRF-Chem) (Grell et

al. 2011; Grell et al. 2005), it could cause incorrect interpretation of smoke-induced aerosol loading and distribution in the atmosphere.

This work presents an algorithm for resolving the emission biases caused by cloud cover, satellite off-nadir observation insensitivity, and satellite observing gaps at equatorial region over Africa. We will test and evaluate our algorithm over the northern sub-Saharan African (NSSA) region where biomass combustion is a large contributor to gaseous and particulate emissions. Our previous study using WRF-Chem simulation and satellite data analysis reveals the intense natural or man-made burning of grassland, cropland, shrubs and other woody vegetation in dry season (October to March) over NSSA extends from $5°S$ to $5°N$ (Yang et al. 2013). From the equator to $10°N$, smoke particles can be mixed well with Saharan dust near the surface, and may be transported above dust layer at 700 hPa or higher altitude (Yang et al. 2013). In addition, a sensitivity study using seven different fire emission inventories to estimate the effects of smoke emission uncertainties on aerosol loading and aerosol radiative effects was done over NSSA biomass burning region (Zhang et al. 2014). The results show that smoke emissions can differ up to a factor of 12 over NSSA, which can lead to the difference in estimate of smoke instantaneous radiative effects by a factor of 33 (Zhang et al. 2014). In this work, we will study the uncertainties due to the satellite-based fire detection limitations posed by cloud cover, off-nadir view, and orbit gaps by focusing on the analysis of Fire Energetics and Emissions Research (FEER) emission inventory over NSSA.

Our correction algorithm is applied and evaluated for the FEER global daily pixel level data with 1 km resolution (FEERV1.0-Mp6) in January 2010 (a high fire occurrence month over northern Africa) is used as a base emission inventory. Hereafter, the original emission is called old inventory, while the emissions corrected by our method is named new, and the emissions calculated by multiplying the new and old monthly ratio to the old emission inventory is named as "scale old". All three inventories are applied over NSSA to the WRF-Chem model in January 2010 and evaluate our correction method. The evaluation is done by investigating particle loading in the atmosphere caused by biomass burning in the region. Since 5-10% of the total smoke aerosol mass is contributed by BC and 50-60% is from organic carbon (OC) (Reid et al. 2005; Tosca et al. 2014), only BC and OC from smoke particle emissions are treated as smoke emissions in this study. No other aerosol sources are considered in the model simulations, which is similar as our past work (Yang et al. 2013; Zhang et al. 2014).

This paper has six parts. In Chapter 2, we briefly review a history of fire and human activity in northern Africa and fire emission construction and correction based on satellite observations. In Chapter 3, we describe the data and model used in this study. Then, we present the emission correction method and its model validation in Chapter 4 and Chapter 5. A summary and discussions about this work are contained in Chapter 6.

# Chapter 2 Biomass Burning History and Emission Estimation

## 2.1 History of Fires and Connection with Human Activities

The occurrence of fires is believed to be accompanied with the gradual appearance of plants on Earth. Plants provide a significant amount of combustible organic matter for fire fuels since the Silurian Period, 420 million years ago (Andreae 1991; Bowman et al. 2009; Scott and Glasspool 2006). The advent of grazers on the Earth altered the relatively simple relationship between plants and wildfires by their consumption of combustible material (Andreae 1991; Schüle 1990). After dinosaur dominance and demise and hominids' evolution caused fire frequency changes, Earth's ecology has become profoundly affected by human-caused fires (Andreae 1991; Bowman et al. 2009).

Though insufficient geological and historical records of fires make it difficult to establish a quantitative analysis of biomass burning, measurements of charcoal and elemental carbon in sedimentary archives have shown that human activity has always been clearly connected with fire regimes (Andreae 1991; Andreae and Merlet 2001; Bird and Cali 1998; Power et al. 2008). On the African continent, human-ignited fires happen almost every day (Crutzen and Andreae 1990), which are believed to play important roles in agriculture and economy. Biomass burning activities include deforestation, shifting agriculture, agricultural waste burning, cooking, and heating (Andreae 1991; Crutzen and Andreae 1990). Large amounts of trace gases and particles are emitted from widespread burning, affecting atmospheric chemistry and Earth's energy balance.

## 2.2 Background of Emission Estimation

The release of particulate or trace gas amount from open combustion is proportional to the amount of dry fuel burned, and the two variables are usually connected by emission factor (EF) (Darmenov and da Silva 2013). The total emission $M_s$ of a particulate or trace gas species *s* can be expressed as (Darmenov and da Silva 2013):

$$M_s = \beta_s \cdot M_{dry} \quad (1)$$

where $\beta_s$ is EF of species *s*, in unit of grams of *s* per kg of dry fuel burned (Andreae and Merlet 2001), and $M_{dry}$ is the amount of dry fuel burned.

Though emissions estimated by aggregating individual fires from a few to hundreds of kilometers spatial resolution and monthly, daily, even hourly temporal resolution is crucial for regional and global transport and climate models (Darmenov and da Silva 2013), the earliest biomass burning emission studies indeed started from the lab experiment investigation of EF and calculated total emission based on equation ( 1 ). The pioneering work of emission estimation by Darley et al. (1966) used a burning tower simulating the open combustion situation at the University of California at Riverside. The associated gas sampling and analysis instruments, which measured every 5 seconds, were placed in the stack of the tower to gather concentrations of hydrocarbon, CO, and $CO_2$. The agricultural wastes burned in their experiments included field crops (e.g. barley, cotton, and rice), fruit, and nut crops (e.g. almond, apple, and apricot) collected from the San Joaquin Valley and San Francisco Bay Area of California. Data were firstly

integrated every 20 seconds throughout a fire, then the results were added together to calculate the EFs of hydrocarbon, CO, and $CO_2$ in unit of pounds per ton of agricultural wastes burned. Though their paper did not describe the data source of burned agricultural fuels, they did mention that they had records of yearly wastes burned amount (including 121,115 tons fruit prunings, 1,632 tons barley straw, and 28,140 tons native brush) in the San Francisco Bay Area before 1966. Their study reported that the total hydrocarbon emission from the annual burning of the three agricultural wastes in the San Francisco Bay Area was about 950 tons. The emission calculation was done through multiplying the maximum yield of hydrocarbon per ton by tonnage of the three agricultural fuels (Darley et al. 1966).

EF in ( 1 ) is an important uncertainty in quantifying biomass burning emissions because of its highly spatial and temporal variable nature (Darmenov and da Silva 2013; Giglio et al. 2006b; Seiler and Crutzen 1980). Even for the same biome, the EF could vary substantially (Van Leeuwen and Van Der Werf 2011). Moreover, the field measurements of EF may not provide a representative value of the realistic fires (Darmenov and da Silva 2013). Fire emissions from burning agricultural wastes and the corresponding EFs were systematically investigated in lab experiments in the 1960s and 1970s (Boubel et al. 1969; Darley et al. 1966; Gerstle and Kemnitz 1967; Sandberg et al. 1975). Field measurement was gradually adopted in fire emission investigations in the late 1970s. By collecting trace gas samples in stainless containers in flights through two smoke plumes, Crutzen et al. (1979) measured and summarized the gas ratios to $CO_2$. The emission ratios were then used to roughly estimate emission of trace gases from global biomass

burning by multiplying them to the gross $CO_2$ amount (estimated as $2–4 \times 10^{15}$ g C $yr^{-1}$) (Seiler and Crutzen 1980). This approach was followed by most of the early studies in which emission of a certain species is estimated by multiplying the corresponding EF for that species with known gross fuel amount or $CO_2$.

The formula to estimate annual total dry biomass burned in a biome is proposed by Seiler and Crutzen (1980):

$$M_{dry} = A \cdot B \cdot \delta \cdot C \text{ [g dry matter per year (g dm } yr^{-1})] \quad (2)$$

where $A$ is total land area burned annually ($m^2$ $yr^{-1}$), $B$ is the average organic matter density for each biomes (g dm $m^{-2}$), $\delta$ is the ratio of above-ground biomass to the total average biomass $B$, and $C$ is the fraction of the above-ground biomass that is burned (often referred to as combustion completeness or the combustion factor). Seiler and Crutzen (1980) also summarized parameters in equation ( 2 ) from past literature for different types of biome and estimated the global annual total dry fuel burned.

The first monthly comprehensive database that describes the spatial distribution of global fire emission was presented by Hao and Liu (1994). Their study discovered areas with high frequency burning in the tropics and the peak burning months in different parts of world. Their study was, however, based on the ground-based reports of biomass burning amount in tropical America, Africa, and Asia during the 1970s, and not estimated for any particular year.

Emission inventory at higher temporal resolution (e.g. daily or hourly) was not available until the satellite detection of land surface was made possible. Since the first weather satellite launched on 1 April 1960 by NASA, the development of satellite technology makes quantitative detection of fires over the globe possible (Polivka 2015). While operational detection of fires from satellites started in late 1980s and early 1990s (Flannigan and Haar 1986; Prins and Menzel 1992; Prins and Menzel 1994; Robinson 1991), the first operational and global estimate of fire emissions, namely, Fire Locating and Modeling of Burning Emissions (FLAMBE), didn't start until the 21$^{st}$ century (Reid et al. 2004). FLAMBE provides global hourly emission with 1–5 km spatial resolution based on fire hotspot data detected by Geostationary Operational Environmental Satellites (GOES) and polar orbiting satellite MODIS (Reid et al. 2005; Reid et al. 2004; Reid et al. 2009). Several other emission inventories with high spatial and temporal resolution were subsequently developed in the past few years (Darmenov and da Silva 2013; Ichoku and Ellison 2014; Ito and Penner 2004; Kaiser et al. 2012; Reid et al. 2009; van der Werf et al. 2010; Wiedinmyer et al. 2011).

While satellite remote sensing is valuable for charactering the spatial and temporal variation of fires and thereby estimating emissions through ( 1 ) and ( 2 ), their advancement also lead to new ways to estimate fire emission, in particular, after the concept of fire radiative energy power (FRP) was introduced in late 1990s (Kaufman et al. 1998) and realized with MODIS in early 2000s (Ichoku and Ellison 2014; Justice et al. 2002). Consequently, two approaches are commonly adopted to use satellite data to

estimate the amount of aerosol or trace gas species emitted from biomass burning: (1) bottom-up method based on the burned area, and (2) top-down method using FRP measured by passive remote sensing instruments.

## 2.3 Bottom-up (burn area) Method

Based on equations ( 1 ) and ( 2 ), the total emission $M_s$ of a particulate or trace gas species $s$ can be expressed as:

$$M_s = \beta_s \cdot A \cdot B' \cdot C \quad (3)$$

where $B'$ is the aboveground biomass density (the product of $B$ and $\delta$). In the early publications, the dry biomass burned was derived from the total biomass density (aboveground and underground) (Hao et al. 1990; Seiler and Crutzen 1980).

Combustion completeness is the fraction of actual fire-consumed fuel to total available fuels. It is highly dependent on the type, spatial arrangement, and moisture content of the fuel (Ito and Penner 2004). Measurements of combustion completeness, $C$, are achievable through measuring pre-fire fuel mass and post-fire residual biomass (Shea et al. 1996). Obvious seasonal changes of C were observed in a Zambian savanna, and found to be highly dependent on vegetation moisture content (Hoffa et al. 1999). Previous literatures show average combustion completeness of fine dry fuels and coarse fuels in forests is $0.90 \pm 0.10$ and $0.27 \pm 0.09$, respectively (Ito and Penner 2004). As for fine fuels in woodlands, *C* is mostly affected by the percentage of tree cover. The average combustion

completeness for coarse fuels in woodlands is $0.30 \pm 0.20$ (Ito and Penner 2004). In general, coarse and wet fuels burn less completely than fine and dry fuels (van der Werf et al. 2006), as expected.

In deciding fuel loads, three approaches are commonly used in recent investigations (Hoelzemann et al. 2004). The first method develops a fuel load map from herbaceous and tree-covered land biomass density data sets as well as three different vegetation cover data (Ito and Penner 2004). The second approach uses passive remote sensing data. The accumulated normalized difference vegetation index (NDVI) derived from Advanced Very High Resolution Radiometer (AVHRR) Global Area Coverage (GAC) data was used to derive fuel load in Sudanian Savanna, Guinean Savanna, humid Miombo, dry Miombo, and Southern Africa Savanna (Barbosa et al. 1999). The third method that is used most frequently applies vegetation models to determine fuel load. Hoelzemann et al. (2014) used Lund-Potsdam-Jena Dynamic Global Vegetation Model (LPJ-DGVM) to simulate fuel load globally.

Burn area is an important source of uncertainty for estimating dry mass burned in equation ( 3 ). The research of burned area estimation started in the 1980s, primarily based upon ground reports (Detwiler et al. 1985; Houghton et al. 1985; Seiler and Crutzen 1980). The importance of burn area in estimating pyrogenic gaseous and aerosol emissions has prompted the development of a variety of satellite-based approaches for mapping burned areas (Giglio et al. 2009). Remote sensing products started to be adopted

in estimating burned area in the late 1980s and widely used since 2000 (Barbosa et al. 1999; Cahoon Jr et al. 1994; Dwyer et al. 2000; Mouillot et al. 2014).

There are two methods that are often used to estimate burn area $A$ in equation ( 3 ). The first is the burn scar approach that estimates the burned area by studying land surface changes before and after fires. Because the burn area is an accumulated result from fires over a certain time period, it is very useful for estimating total emission for the fire events but lacks the characterization of temporal variation of fire emissions within the time period of a fire event. Cahoon Jr et al. (1994) identified 14.45 million ha of east-Asian boreal forest burned in 1987 through unsupervised minimum distance classification to AVHRR imagery. Barbosa et al. (1999) estimated burned area of Africa from 1981–1983 and 1985–1991 by analyzing the AVHRR global area coverage images at 5 km resolution to examine the reflectance, brightness temperature, and vegetation index changes. A number of global burned area products has also been developed (Roy et al. 2002; Simon et al. 2004; Tansey et al. 2004). Hoelzemann et al. (2004) used the burn scar data to estimate monthly biomass burning emissions. Except for using standard remotely-sensed indicators (surface reflectance, surface temperature, NDVI, etc.), active fire data are also combined with standard remotely-sensed indicators in some mapping methods for burned areas (Giglio et al. 2009). Global monthly burned area at $0.5° \times 0.5°$ spatial resolution from July 1996 to mid-2000 were provided using multi-sensor data (Giglio et al. 2010). The main burned area data source was 500-m burned area maps derived from MODIS imagery and 1-km MODIS active fire observations (Giglio et al. 2009; Mouillot et al. 2014). Prior to the MODIS era, the burned area data were extended by using Tropical

Rainfall Measurement Mission (TRMM) Visible and Infrared Scanner (VIRS) and Along-Track Scanning Radiometer (ATSR) active fire data (Giglio et al. 2010; van der Werf et al. 2010). These data have been used to develop the third version of the monthly Global Fire Emissions Database (GFED3).

The second approach for estimating the parameter A in equation ( 3 ) is through retrieval of fire size and temperature of fires, so the approach is called active fire method. The fire area is estimated using fire hotspot detection. Since fire location and time are both available from satellite products, this approach enables instant emission rate estimation. FLAMBE uses the instantaneous sub-pixel fire size and fire temperature from GOES satellite products based on the Dozier's two channel method (Dozier 1981; Reid et al. 2009). In the hour of the fire detection, the hourly emission product is formed using GOES sub-pixel fire size. When GOES fire product is not available, area burned for each MODIS fire-detection is estimated at 62.5 ha and this value is further scaled diurnally based on the Wildfire Automated Biomass Burning Algorithm (WF_ABBA) based step function (Giglio 2007; Theisen et al. 2002; Zhang and Kondragunta 2008). Fire INventory from NCAR (FINN) also used MODIS active fire products (Giglio et al. 2006a) for fire area estimation. For each detected active fire, the burned area is estimated as 0.75 $km^2$ for fires located in grasslands/savannas and 1 $km^2$ for other regions (Wiedinmyer et al. 2011). This value is further scaled based on the percent of bare cover from MODIS Vegetation Continuous Fields (VCF) product. The daily global emission estimate is then provided.

Table 1 shows the detail comparison of the data sources for common parameters needed in bottom-up estimate of fire emissions, as well as how the sampling biases caused by cloud or satellite geometry were considered in several emission inventories. The emission inventories GFED4 and FINN are estimated with special consideration of undetected fires in the satellite swath gap region. However, none of these estimates corrected the biases caused by large VZA and cloud cover.

## 2.4 Top-down (Fire Radiative Power) Method

Part of the heat released by fire combustion is added to the environment, the other part is released primarily as infrared radiation (Darmenov and da Silva 2013). A linear relationship between the time-integrated Fire Radiative Energy (FRE) and the dry fuel burned has been demonstrated (Wooster 2002), and this linear relationship forms the basis for top-down approach emission estimation (Darmenov and da Silva 2013):

$$M_s = \alpha \cdot \beta_s \cdot \int_{t_1}^{t_2} F(t)dt \qquad (4)$$

where $F(t)$ is FRP in unit of MJ $s^{-1}$ or MW, $\alpha$ is a constant that connects Fire Radiative Energy (FRE) and consumed dry mass amount. According to equation ( 4 ), the emission rate $E_s$ of species $s$ per unit area that can be used in chemical transport model can be written as

$$E_s = \frac{\Delta M_s}{\mathrm{A} \cdot \Delta \mathrm{t}} = \alpha \cdot \beta_s \cdot \frac{F}{A} \qquad (5)$$

$A$ is the area of satellite pixel, and $F/A$ is FRP area density.

The advantage of top-down approach is the direct link between satellite measured FRP and dry mass burned which is, in turn, related to emission. Ichoku and Kaufman (2005) derived a smilar equation to equation ( 1 ) by replacing EF with emission coefficient ($C_e^s$, expressed in kg $MJ^{-1}$) and $M_{dry}$ with FRE. Thus emission rate $R_s$ of species $s$ (expressed in kg $s^{-1}$) is proportional to the product of emission coefficients and FRP.

$$R_s = C_e^s \cdot F \qquad (6)$$

The main data for deriving $C_e$ are satellite measurements of FRP and aerosol optical depth (AOD), and the Modern Era Retrospective-Analysis for Research and Applications (MERRA) wind fields (Ichoku and Ellison 2014).

The direct use of FRP and the availability of global high spatial and temporal resolution FRP data make top-down method to generate more suitable emissions for smoke-emission, chemical transport, and climate models (Ichoku and Kaufman 2005). Even when a fire is actively burning, this method could be used to estimate emissions (Ichoku and Kaufman 2005). However, fires under cloud cover, in satellite swath gap regions, and small fires in large VZA detection regions may cause underestimation of emissions. Table 2 lists data sources and calibration of biases in some emission inventories that used the top-down method.

As shown in Table 2, Global Fire Assimilation System version 1.0 (GFASv1.0) calculates global daily biomass burning emissions based on Terra- and Aqua-MODIS FRP. The emission factors used by GFASv1.0 are based on information from previous studies (Andreae and Merlet 2001; Christian et al. 2003). In GFAS, pixel areas from satellites with valid observations of fire and no-fire are used to calculate FRP density at the grids of $0.5° \times 0.5°$ resolution across the globe. The polar-orbiting satellite geometry causes a "bow-tie effect" (Wolfe et al. 2002), which happens when the satellite scans the same point on the Earth's surface multiple times at scan edge. This effect has been corrected in the FRP density calculation step by GFAS (Kaiser et al. 2012). The cloud-corrected and quality-controlled FRP density data are then used for GFASv1.0 emission calculations. GFASv1.0 emission is however still underestimating biomass burning emissions over Africa when compared with FLAMBE (Zhang et al. 2014).

Quick Fire Emissions Dataset version 2.4 (QFEDv2.4) is a global daily emissions inventory based on Terra- and Aqua- MODIS FRP (Darmenov and da Silva 2013). Fire locations are first mapped to the corresponding vegetation class, and then the EFs are selected (Andreae and Merlet 2001), and FRP are assigned to QFED vegetation type. Global binned FRP and pixel area are used by top-down approach to calculate emissions. In this process, satellite pixels obscured by clouds are treated using the sequential method (Darmenov and da Silva 2013) in QFEDv2.4 to extend the emissions covered by clouds. The sequential method relies on a damped persistence model to estimate current FRP

density in the cloud obscured area based on previous day and current observations. QFED also underestimates the emission as reported in (Saide et al. 2015).

FEERv1.0-G1.0 inventory is also developed based on a top-down approach (Ichoku and Ellison 2014) and is available for public at NASA website http://feer.gsfc.nasa.gov/. Equation ( 6 ) is the fundamental relation used in FEERv1.0-G1.0 algorithm.
The global gridded (1° × 1°) $C_e$ products for smoke total particulate matter (TPM) is first derived based on the method proposed by Ichoku and Kaufman (Ichoku and Kaufman 2005). The FEERv1.0 $C_e$ at 1° × 1° resolution was multiplied by coincident time-integrated FRP data at 0.5° × 0.5° resolution from GFAS (Kaiser et al. 2012) to calculate regional smoke TPM. For different smoke-aerosol components, the FEERv1.0-G1.0 algorithm relies on the EFs (Andreae and Merlet 2001) to convert TPM emissions to various species. Both the FRP and AOD data used to generate gridded FEER.v1 $C_e$ are derived from MODIS on Terra (MOD14 and MOD04_L2) and Aqua (MYD14 and MYD04_L2) satellites. In order to distinguish the background and smoke plume AOD, the MERRA wind vector at 850 hPa dataset is used in the algorithm (Ichoku and Kaufman 2005; Ichoku and Ellison 2014). The wind magnitudes are also used in the FEERv1.0-G1.0 algorithm to estimate the time when the mass of smoke aerosol is emitted by a certain plume. The linear relationship between FRP and the rate of smoke emission is then determined to get the gridded (1° × 1°) $C_e$ products (Andreae and Merlet 2001; Ichoku and Kaufman 2005; Ichoku and Ellison 2014). FEERv1.0-G1.0 is the first biomass burning emission derived from global gridded emission coefficients products. The ecosystem type of active fire is not required to be pre-defined in the algorithm.

From comparisons between different biomass burning emission inventories derived using the top-down method (Table 2), we found none of them considered emission underestimation caused by undetected at off-nadir view. Although they have all corrected cloud cover and swath gaps caused biases, total smoke emission over NSSA in different inventories vary by a factor of 12 (Zhang et al. 2014), demanding for further studies.

Here we will present a method to calibrate the emission biases introduced by (a) satellite limitation in detecting fires under clouds; (b) the lack of fire detection sensitivity at the edge of MODIS scan where viewing angles and MODIS pixel size are bigger than at nadir; and (c) data gaps between MODIS swaths at the ground in low latitude regions. The FEER data family has an inventory FEER-SEVIRIv1.0 (using FRP measurements from the geostationary Meteosat Spinning Enhanced Visible and Infrared Imager (SEVIRI)) that has been employed in our previous work (Zhang et al. 2014) to estimate how the air quality and climate models respond to uncertainties of different emission inventories. In the third part of the study of smoke effects over NSSA, this work will use pixel level FEER BC and OC with 1 km resolution data as the baseline for smoke emission inventory in NSSA.

# Chapter 3 Model and Datasets Description

## 3.1 WRF-Chem Model

The fully coupled meteorology-chemistry-aerosol model WRF-Chem (Fast et al. 2006; Grell et al. 2005) is used in this study to investigate how the method for correcting emission inventory biases may affect the simulation of atmospheric aerosol loading. The model configuration options are listed in Table 3, which are similar to our previous works in the NSSA region (Yang et al. 2013; Zhang et al. 2014). In brief, radiation schemes used in this work including the Goddard two-stream multi-band scheme with ozone from climatology and cloud effects (Chou et al. 1998) for short wave and Rapid Radiative Transfer Model (RRTM) scheme for long wave (Mlawer et al. 1997). The Regional Acid Deposition Model, version 2 (RADM2) chemical mechanism (Stockwell et al. 1990) is adopted in this study. The aerosol modules are Modal Aerosol Dynamics Model for Europe (MADE) (Ackermann et al. 1998) and Secondary Organic Aerosol Model (SORGAM) (Schell et al. 2001). We also used Noah Land Surface Model with soil temperature and moisture in four layers, fractional snow cover and frozen soil physics (Chen and Dudhia 2001). The Yonsei University (YSU) scheme (Hong et al. 2006) is selected as boundary layer parameterization. A sophisticated microphysics scheme, Lin et al scheme (Lin et al. 1983), that has ice, snow, and graupel processes, suitable for real-data high-resolution simulations and New Grell cumulus scheme (G3) (Grell and Dévényi 2002) are used in our model configuration.

The initial and boundary conditions for WRF-Chem model are provided by National Centers for Environmental Prediction (NCEP)/National Center for Atmospheric Research (NCAR) Global Final Analysis (FNL) data. FNL data have been prepared at 00:00, 06:00, 12:00, and 18:00 UTC with 1° × 1° horizontal resolution and 26 vertical levels (Kalnay et al. 1996). A collection of FNL data for this study has been obtained from http://rda.ucar.edu/datasets/ds083.2/. This study focuses on the month of January 2010 with intense biomass burning in NSSA.

The first week in simulation is for model spin-up. A double-nested grid configuration of WRF-Chem model is used in the NSSA region. A fine grid of 130 × 85 points with 27 km grid spacing covering NSSA is nested within a coarse grid of 259 × 133 points of 81 km grid spacing. The lower left corners for these two domains are (21.88°S, 29.42°W) and (13.24°S, 16.55°W), respectively.

The important two components of biomass burning emissions, BC and OC from the fire inventory are input to the model. The emission implementation is the same as our first part of this project work in NSSA (Yang et al. 2013). The highest smoke vertical transportation height is set as 650 m above the surface in the model. The smoke emissions are well mixed in model layers below this height.

## 3.2 AERONET Data

The optical ground-based Aerosol Robotic Network (AERONET) has over 1000 sites established by NASA over the world (Holben et al. 1998). The Sun-sky scanning radiometer in each site measures aerosol optical properties (e.g., Aerosol spectral optical depth, angstrom exponent and aerosol size distribution) (Dubovik et al. 2000). We use both AERONET cloud-screened and quality assured (Level 2.0) AOD data in this study. The uncertainty of AERONET Level 2.0 AOD data is about 0.01–0.02 (Eck et al. 1999; Levy et al. 2010). In order to use AERONET AOD as ground truth in this study and compare it with satellite and model simulation results, AOD at 0.44 μm and 0.675 μm are used to interpolate AOD at 0.55 μm through Angstrom Exponent. Three AERONET sites that are close to the high biomass burning activity region and have valid Level 2 data from January 2003 to January 2016 are selected in this study to evaluate MODIS AOD data. The three AERONET sites are Ilorin (8.3 $°N$, 4.3 $°E$), Djougou (9.8 $°N$, 1.6 $°E$), and Kibale (0.6 $°N$, 30.3 $°E$).

## 3.3 MODIS Data and Processing Method

AOD, fire, and cloud products from MODIS instruments on Terra and Aqua are used in this study. The Terra satellite (launched in 1999) passes by the equator at local time 10:30 am, and the Aqua satellite (launched in 2002) at 1:30 pm. The twin MODIS sensors on Terra and Aqua provide near-global daily observations of the earth at wide spectral range (0.41 to 14.5 μm in 36 channels), broad swath (2330 km) and relatively fine spatial

resolution (250 m to 1 km at nadir) (Levy et al. 2013; Levy et al. 2007; Levy et al. 2010; Remer et al. 2005).

### 3.3.1 AOD, Fire & Cloud Data

At 0.47, 0.55, 0.66 and 2.13 μm wavelengths, the MODIS AOD are retrieved over land, while at 0.48, 0.55, 0.66, 0.87, 1.20, 1.60, and 2.13 μm, the AOD are retrieved over oceans. The newest MODIS Collection 6 (C6) aerosol products have three parts (1) DT over oceans, (2) DT over vegetated/dark-soiled land, and (3) DB over bright desert surfaces (Levy et al. 2013). For MODIS retrieved C6 DT total AOD (at 0.55 μm), the expected error is $\pm\ (0.03 + 5\%)$ over ocean and $\pm(0.05 + 15\%)$ over land (Levy et al. 2013; Levy et al. 2010; Remer et al. 2008). The highest quality DB total AOD (at 0.55 μm) absolute uncertainty is $0.03 + 20\%$ of AERONET (Sayer et al. 2013). In this study, we use both Terra (MOD_04) and Aqua (MYD_04) C6 0.55 μm AOD data with 10 km resolution to evaluate the model performance after applying the emission correction method.

Active fire products from MODIS are based on the algorithm that uses brightness temperature at 3.9 μm and 11.0 μm wavelength to detect active fires and other thermal anomalies (Giglio 2010; Justice et al. 2002). Each MODIS Level 2 fire product granule covers a region of approximately $2340\ \times\ 2030$ km in both the along-scan and along-track directions. It has a 1 km resolution at nadir, and contains the FRP and flags that mask fires and other relevant pixels (Giglio 2010). The fire pixel counts ($N_f$), the number of pixels obscured by clouds ($N_c$), and the total number of observed pixels ($N_t$) in a

certain study region can be obtained from Aqua MODIS Level 2 fire products (MYD_14). Aqua MODIS Level 1 (MYD_03) geolocation data with 1 km resolution is used to determine the location of each fire pixel.

MODIS Level 2 daily cloud product MOD/MYD_06 data (Ackerman et al. 1998) from Terra and Aqua satellite is used in this study for MODIS AOD evaluation and emission correction algorithm. MOD/MYD_06 products provide cloud fraction at 1 and 5 km resolution. The MODIS Level 2 MOD/MYD_35 cloud mask data are used in the emission merge step.

### 3.3.2 MODIS AOD Data Processing

Since our current emission correction method aims at NSSA land region, only MODIS land AOD are used in this study to evaluate if our method for emission correction renders simulation by WRF-Chem. Several quality assurance (QA) filters are used in this work to reduce DT and DB AOD errors.

MODIS Level 2 DT AOD over land includes QA flags in four categories: "No Confidence," "Marginal," "Good," and "Very Good." A previous study shows when using only "Very Good" MODIS C5 retrievals, the global fraction of MODIS land DT AOD within the expected uncertainty envelope ($0.05 \pm 20\%$ of AERONET AOD) improves from 62% to 67% (69%) for Terra (Aqua), and the correlation between MODIS and AERONET is greatly improved (Hyer et al. 2011). When the scattering angle (SA) is very big (for example, greater than 170°), the matched MODIS-AERONET data within

target accuracy are even less than 50% (Vermote and Roy 2002). Thus, we also eliminate any DT data with SA greater than 170°, and use DT AOD data that are in the "Very Good" category. AOD bias from cloud contamination is reduced by using data only with cloud fractions equal to 0. We also exclude AOD retrievals without adjacent valid retrievals using buddy check. The 3 × 3 pixels around a valid AOD retrieval are searched (Hyer et al. 2011; Zhang and Reid 2006). Table 4 shows MODIS DT data filters and corresponding data loss over the study region.

DB data QA processes are similar to DT. AOD retrievals at 0.55 μm confidence flag have four classes: "No Confidence," "Marginal," "Good," and "Very Good." An evaluation study of MODIS DB data over northern Africa using AERONET observational data shows adopting "Very Good" QA may reduce error (Shi et al. 2013) even though there are limitations. We thus used QA in the "Very Good" category in this study. Cloud contaminated data are removed when $F_{cld}$ is greater than 60%. Except for buddy check, standard error (STE) check was also performed for DB data. The STE was calculated for every 3 × 3 pixel around a valid AOD retrieval (Shi et al. 2013). Terra and Aqua DB QA filters and data loss are listed in Table 5.

Averages of DT and DB AOD are calculated and defined as "DTB" in this study. Figure 1 shows the monthly average of Terra DT, Aqua DT, Terra and Aqua mean DT, Terra DB, Aqua DB, Terra and Aqua mean DB, Terra DTB, Aqua DTB, Terra and Aqua mean DTB AOD at 0.55 μm before, (a1)–(a9), and after QA procedures at the WRF-Chem grid, (b1)–(b9). There are a total of 18 groups of MODIS AOD products in Figure 1.

AERONET monthly AOD at 6 stations in the study region are also overlaid in Figure 1(b9). AERONET Level 1.5 cloud screened data are used in order to obtain the real time data (Ichoku et al. 2002). AERONET daily average data are computed for days when there were at least 2 times of observation. The monthly average AERONET AOD is calculated when the valid daily data number is greater than 5 days in January 2010. MODIS Level 2 AOD data are assigned to WRF-Chem grid according to the distance between satellite pixels and model grids. The monthly average of MODIS AOD is calculated when number of days with valid data is greater than 5. Before QA, Terra MODIS AOD tend to be higher than Aqua MODIS AOD between 2°–11°$N$. The QA process removes certain amount of data in the study region no matter which group of AOD is checked. Nonetheless we could always see the biomass burning caused a high AOD belt in the map (0 °–10°$N$).

The monthly average AERONET AOD is consistent with MODIS AOD at the off-burning region. However, the AERONET AOD at Ilorin station (which is closest to the intense biomass burning region) is higher than monthly MODIS AOD. The 18 groups of MODIS AOD show differences. In order to decide which group of MODIS AOD data should be used for model performance evaluation, we evaluated MODIS AOD before and after QA procedures using the available 2003–2016 January AERONET data. The selected AERONET stations are located within the intense biomass burning belt (0°–10°$N$) in NSSA. The 2003–2016 time period is selected because MODIS C6 January data are currently available for 2003–2016 from Aqua, and 2000–2016 from Terra. AERONET Level 2 data is used in MODIS AOD evaluation in this study (Shi et al.

2013). The satellite and AERONET collocation follows the spatiotemporal method proposed by Ichoku et al. (2002). The sunphotometer data are selected within the temporal window of ±30 min of satellite overpass time. A 5×5 MODIS pixel window is selected spatially with AERONET site in the middle. The collocated data statistics are calculated only when there are at least 5 valid data points of the MODIS 5×5 retrievals and 2 valid data points of the 4 to 5 AERONET data within ±30 min (Levy et al. 2010).

Figure 2 shows a scatter plot of daily average MODIS Terra DT, Aqua DT, Terra and Aqua mean DT, Terra DB, Aqua DB, Terra and Aqua mean DB, Terra DTB, Aqua DTB, Terra and Aqua mean DTB AOD, compared with AERONET Level 2 AOD at 0.55 μm before, (a1)–(a9), and after QA, (b1)–(b9). The scatter plot contains traditional parameters for satellite data evaluation using AERONET. The regression equation $AOD_{satellie} = b + a \cdot AOD_{aeronet}$ calculates the diagnostic values and describes the quality of the satellite retrievals against the "true value," AERONET AOD (Shi et al. 2013). The root-mean-square errors (RMSE) are calculated through the same equation in the study of Shi et al. (2013).

$$RMSE = \sqrt{\frac{1}{n}\sum_{n}(AOD_{aeronet} - AOD_{satellite})^2} \quad (7)$$

It indicates the bias of the satellite retrievals against AERONET. For comparisons between different groups, the correlations between MODIS and AERONET all increased after QA except for groups 1, 8, and 9. The RMSE is decreased after QA except for

groups 1, 2, 3, and 9. In order to get a relatively large data coverage from MODIS to be compared with the model results, Terra and Aqua DB mean AOD after QA are used as the best AOD data in evaluating model performance over NSSA in January 2010. In addition to having a relatively large spatial coverage, this group of AOD data also has high correlation and low RMSE. As for the data evaluation at Aqua gaps and large VZA regions, Terra ADO is required. Considering the low RMSE and high correlation, Terra DB after QA is selected as the "truth" for model evaluation at Aqua gaps and large VZA regions.

## 3.4 Emission Data

FEER version 1.0 pixel level data (FEERV1.0-Mp6) contains emission data for each detected fire pixel with 1 km resolution. The resolution is consistent with the FRP data from the newest MODIS C6 active fire product (Giglio et al. 2016) used by the FEER group.

### 3.4.1 Gridding of pixel-level emission

For each day, the pixel level 1 km emission data were lumped into four groups according to FRP sources: (1) Terra Daytime, (2) Terra Nighttime, (3) Aqua Daytime, and (4) Aqua Nighttime. Four emission files at WRF-Chem grid are generated for each day. The regrid progress was simply based on finding the nearest distance between satellite pixels and the WRF-Chem grid. For satellite pixels within a certain WRF-Chem grid, the corresponding emission $E_i$ is assigned to this grid. For each WRF-Chem grid cell j:

$$E_j = \sum_{i \in j} E_i \quad (8)$$

For coarser-resolution model domain, Earth System Modeling Framework software is used to interpolate higher resolution (27 × 27 km) data to coarse resolution (81 × 81 km) data. For outside domain regions that do not overlap with the nested domain, the same method is used for coarse domain as for the finer domain.

### 3.4.2 Emission Merging

We use optimal interpolation to merge emission values from different satellite products (Terra and Aqua, day and night) in this study to obtain a combined product for each day (Kaiser et al. 2012). The weight is based on the ratio of satellite observed area to each model grid area. Before the interpolation, the overlapping pixels in dataset have been deleted (fires can be detected multiple times in subsequent scan lines because of the bowtie effect). The fraction of satellite observed area that can possibly be valid for fire detection by the satellite in each of the model grid $f_j$:

$$f_j = \frac{\sum_{i \in j} S_i . cos^2(\theta_i)}{\varsigma_j} \quad (9)$$

$S_i$ is the pixel area for pixel $i$, $\theta_i$ is the VZA, and $\varsigma_j$ is the model grid area. Parameters in equation ( 9 ) are calculated for all satellite pixels that are valid either fire or no-fire detection. Invalid satellite pixels caused by water, ice, and cloud cover are not accounted

for in equation ( 9 ). MODIS L2 MOD/MYD35 day and night cloud mask data with 1 km resolution are used to distinguish water, ice, and cloudy pixels. The underlying assumption is that, within the same model grid, the fire spatial distribution is the same, and therefore, satellite-based fire spatial distribution in cloud-free, water-free, and ice-free regions can be applied to the areas where fires cannot be detected.

An equation similar to the equation (10) in Kaiser (2012) is used to merge several gridded satellite products. The merging process is necessary to get a combined data for each grid from several simultaneous satellite observations on the same day. The diurnal profile based upon the three hourly variability in fire emissions derived from GOES and MODIS is then applied in our emission rate data (Mu et al. 2011; Zhang et al. 2014). The emission rate for each hour in every three-hourly interval is kept as a constant.

# Chapter 4 Emission Correction Method

Figure 3 shows the flow chart of our emission correction method. It starts with the top-down emission inventory FEERV1.0-Mp6, followed by two correction steps. One correction is for the cloud cover condition, and another is for the large view-angle effect and satellite orbital gaps. Figure 4 shows the time series of inner domain total BC and OC baseline (old) emission from different satellite platforms on day and night. The largest daily emission retrieved in January is from Aqua daytime products with a monthly average emission value of 89.82 Gg, while monthly average emission retrieved from Aqua nighttime, Terra daytime, and Terra nighttime is 3.98, 33.02, and 5.10 Gg, respectively. Thus, the development of emission correction algorithm in this paper is based on Aqua daytime observations first.

Figure 5 shows Aqua-MODIS true color image overlaid with the satellite detected daytime fires (red dots), (a)–(b), and Terra Aqua mean DB AOD, (c)–(d), on 1 and 2 January 2010. The white solid, dot, and dash lines in Figures 5 (c)–(d) stand for Aqua swath borders, $\theta$ = 35 ° tracks, and satellite nadir view orbits. As discussed in Chapter 3, FEERV1.0-Mp6 is prepared based on MODIS detected FRP. The FRP data have three main limitations related to satellite detection of ground fires. First, the satellite fire detection is less sensitive in the off-nadir views. As shown in Figures 5 (a)–(b), when the view angle is large, there are fewer fires detected by satellite (yellow and red boxes). In contrast, the AOD retrievals reveal that nearly the same amount of smoke AOD exists in

the off-nadir regions as in the nadir views (Figures 5 (c)–(d)). The same region's fire density is clearly higher on 2 January when compared with 1 January (yellow box in Figures 5 (a)–(b)). Fires in the study region are mostly lit by farmers and herders. The fire distribution related to agricultural activity should not vary so much in two continuous days. Second, the sun-synchronous orbits of the Terra and Aqua satellites have observation gaps at the equator in one day when successive satellites pass by the same latitude. As marked in Figure 5 (a), there is no fire detection available at all at the gap between two swaths. Similar as off-nadir fire detection limitation, the initial analysis of satellite gap areas in a particular day shows that the gap areas can contain significant amount of fire activities that are detected either one day earlier or after this particular day. Even in same day, valid and large Terra- and Aqua-MODIS AOD retrievals are still available in off-nadir and gap regions, which contrasts with the few (zero) fires being detected these regions. A previous study based on 15-min temporal interval SEVIRI FRP data records over Africa (Roberts et al. 2009) also shows that such MODIS detected appearance and disappearance of fires at the satellite detection gap or off-nadir on continuous days are not authentic. Third, MODIS is only able to detect fires at cloud-free areas at the equator (Freeborn et al. 2011; Kaiser et al. 2012). As marked in Figure 5 (b), the distribution of fires can be interrupted due to cloud cover. Because of these limitations pertinent to satellite fire detections, FRP are likely underestimated. The emission correction is necessary to compensate the emissions from undetected fires.

The bias in fire detection is also exemplified in Figure 6. Figure 6 shows time series of Aqua gathered $N_t$ (a), daytime averaged VZA (b), and the Fraction of Fire (FOF) (c) in an

arbitrary WRF-Chem grid (9.0 °$N$, 9.4 °$W$) over NSSA in January 2010. In each model grid cell, FOF is defined as the ratio of $N_f$ to the clear sky pixels number ($N_{clr}$):

$$FOF = \frac{N_f}{N_{clr}} = \frac{N_f}{N_t - N_{cld}} \quad (10)$$

$N_t$ is the total number of observed pixels and $N_{cld}$ is cloudy pixels count.

Figure 6 indicates when the scan angle increases the total fire pixel number decreases. In addition, this view geometry and total pixel number relationship affects FOF in our case. High FOF values appear when a relatively small VZA occurs. We found this MODIS fire detection efficiency bias is similar to a previous study using AVHRR satellite observation (Heald et al. 2003). Following the previous study (Heald et al. 2003), we assume here for each model grid, the probability of fires at cloudy pixels is the same as at cloud-free pixels, at least in the scale of model grid box (~27 km).

## 4.1 Emission Correction for Cloud

Every daytime pixel from Aqua-MODIS Level 1 MYD03 product is assigned to the corresponding model grid to calculate daily mean VZA at each model grid. The daily average total pixel number, cloud pixel number, and fire pixel number are calculated for each WRF-Chem grid, as described above. Average daytime cloud fraction at each model grid is also calculated using Aqua-MODIS Level 2 MYD06 products.

Considering fire activity is possible in persistently cloudy regions (Heald et al. 2003; Robinson 1991), the current method for compensating fire pixels obscured by clouds assumes that fire frequency in a cloudy region is the same as the cloud-free areas within the same model grid (Cardoso et al. 2003; Giglio et al. 2003; Giglio et al. 2006a; Roberts et al. 2005; Schroeder et al. 2008). Accordingly, this study corrects emission bias caused by cloud using the following equation using

$$E = E^0 + E^0\left(\frac{N_t \cdot F_{cld} \cdot FOF}{N_f}\right)$$
$$= E^0\left(1 + \frac{N_{cld}}{N_{clr}}\right) \quad (11)$$

In (11), $E^0$ is the original emission at WRF-Chem grid, $E$ is the new emission after cloud correction and $F_{cld}$ is the model grid cloud fraction detected by MODIS.

## 4.2. Emission Correction for Large View Angle and Gap Filling

We assume that the emission estimation biases are minimal for the satellite detections where VZA is less than the threshold $\theta_t = 35°$. Hence, for any grid with $> \theta_t$, we replace $E$ of that grid with forward or backward two days' $E$ at the same grid that has the smallest daily $\theta$ among five days centered at the target date, otherwise no correction is made and the original $E$ is kept. The VZA threshold of 35° and the time window of 5 days are selected because at any WRF-Chem grid of the study region, our analysis shows the observation with VZA less than or equal to $\theta_t$ appear at least once in any continuous

5 days. This will make sure there is no data gap in those 5 days. In addition, the rapid variation of fires would result in low confidence if we replace the off-nadir emission with data over 5 days. After getting the new emission, we calculated the daily domain emission ratio between the new and old emission over the study domain. Using this ratio, we built another emission inventory named “scale old.” Scale old emission is created by applying the new and old ratio to the original emission.

# Chapter 5 Emission Correction Results Evaluation

The application of our emission correction algorithm is to provide an improved biomass burning emissions for regional air quality and climate model. Thus, we applied the emission correction method to FEERV1.0-Mp6 pixel level 1 km resolution emission data for January 2010. Then, we applied the old, spatially continuous new and "scale old" emissions into the WRF-Chem model to simulate and discover how the aerosol loadings over the NSSA region in January 2010 respond to three different emissions.

Figures 7 (a)–(l) show three sets of BC+OC emissions and the WRF-Chem simulated column total AOD at 0.55 μm on the same days as in Figure 5. The new emission distribution corresponds well with the smoke locations observed from satellite true color image (Figure 5 (a) and (b)). It is clearly shown that the data gaps at the Aqua satellite off-nadir have been filled in the new emission while the "scale old" emission simply increased emission amount to the old one. The total BC+OC emission amounts in the study region improved from 41 (40) Gg to 92 (82) Gg for 1 (2) January 2010. Though in the "scale old" case the total emission amounts are increased to the same values as in the new case, the AOD distributions simulated by WRF-Chem with the new emission are closer to Figure 5 MODIS AOD distributions. The new emissions have improved spatial pattern of AOD distributions and reduced biases in satellite off-nadir and gap regions.

This indicates that the emission correction method works for NSSA when the corrected emission inventory is applied in the weather forecasting model.

The effects of the new emission to the model are further illustrated in Figure 8. Based on the two-day simulation results, Taylor diagrams in Figure 8 show how the emission correction method improves WRF-Chem simulated AOD. The centered root-mean-square (RMS) difference between WRF-Chem and MODIS AOD is proportional to the distance to the point on the x-axis identified as "REF" in Figure 8. "REF" is our "true value" (MODIS retrievals). When comparing model simulated daily AOD (08:00–20:00) with MODIS Terra Aqua mean DB AOD in NSSA high fire frequencies region (0 °–10 °$N$), our new case has reduced the center RMS error and standard deviation difference and increased correlation. The "scale old" case only resulted in closer standard deviation values to the MODIS retrievals.

Figure 9 shows the monthly (January 2010) average column total AOD at 0.55 μm simulated by WRF-Chem using three different emissions. Since our study aims at stressing the model performance enhancement resulting from emission improvements, we did not consider other aerosol sources in the model. Thus, the model results did not show dust loading at the northern part of NSSA. Though the overall magnitude is small over the study domain, the new simulated AOD pattern has certain improvements in some areas compared to the "scale old" case. When compared with monthly Terra Aqua mean DB AOD (Figure 1 (b6)), our simulation using new emissions captures the relatively high AOD pattern in the yellow box marked region (Figure 9 (b)). The new emission

improvements to the model performance are also shown in the Taylor diagram of Figure 10. Figure 10 shows WRF-Chem simulated daily column total AOD at 0.55 μm compared with Terra Aqua mean DB after QA (a) and model results compared with Terra DB AOD after QA at Aqua gap and Aqua $\theta > \theta_t$ over high smoke loading regions (b) in January 2010. As shown in Figure 10 (a), the new simulation results are better than the old ones when considering correlation, centered RMS error, and data standard deviation. By comparing new results with "scale old" results, we find the model performance improvement was not simply caused by increased emission amount, but also resulted from spatial filling of emission inventory. Because we filled the emission with forward and backward day's data in Aqua gap in areas with $\theta > \theta_t$, we also evaluated model performance in those areas (Figure 10 (b)). Overall, the new and "scale old" cases are improved from the old one. Though the new and "scale old" cases overlapped in the figure, our day-by-day check shows over half of new case data in January are better than "scale old" results. Figure 11 shows the comparison of WRF-Chem column total AOD at 0.55 μm in whole month of January with Terra DB AOD after QA over intense smoke loading region (0-10°$N$). Overall, new emission has increased WRF-Chem simulation in aerosol loading when compared with old and "scale old" cases.

In order to further investigate the emission correction effects, the model results are evaluated using Cloud-Aerosol Lidar and Infrared Pathfinder Satellite Observations (CALIPSO) Cloud-Aerosol Lidar with Orthogonal Polarization (CALIOP) 5 km aerosol extinction products. Night time CALIOP data on three days were selected when CALIPSO overpassed the Aqua daytime gap on those days and $\theta > \theta_t$ areas. Because

our emission correction methods focus on this area, the vertical profile comparison is necessary to evaluate how the changes of daytime emission affect the model simulations in nighttime hours.

Figure 12 shows the nighttime CALIPSO tracks (blue lines) that pass by day time Aqua large VZA or gap regions (first row) and the comparison of night time CALIOP-derived vertical profiles of AOD (calculated from aerosol extinction coefficient) at 532 nm (second row), WRF-Chem simulated vertical profiles of smoke concentration along the corresponding CALIPSO ground track using old (third row), new (fourth row), and scale old emissions (fifth row). Data from 3, 4, and 22 of January 2010 are shown from the first column to the third column. Due to the cloud cover, lidar signal was lost at some regions. All the model simulated results using different emissions can capture the rough patterns of vertical aerosol profiles. The smoke injection height ranges from 3 to 6 km. It is noted the "scale old" emission has no effect on the aerosol vertical distribution but simply increases the aerosol amount on the basis of old case. The red ovals in Figures 12 (a2), (b2), and (c2) indicate the location where the new emission input changed the model simulated aerosol vertical distributions (changes are shown by red ovals in (a4), (b4), and (c4)). On 3 January 2010, the AOD values marked by the red oval region are around 0.005-0.008. The data range is very similar to the values on the left side of the red oval in the figure. The new emission has increased the simulated aerosol vertical loading over this region and the magnitude is close to the aerosol concentration on the left side of the red oval in the figure. However, the old and "scale old" simulated aerosol concentrations are relatively low when compared with the new result. The new emission enhancement to

the model simulation is further shown in the case on 4 January 2010. There are high AOD values over the red oval of Figure 12 (b2). Neither the old nor the “scale old” simulations depicts these high aerosol concentrations. Only the new case simulates the high aerosol loadings in this region. A similar situation of 3 January also happens on 22 January 2010. The red oval in Figure 12 (c2) shows a region with a relatively high AOD that is only captured by the simulation using new emission. According to the vertical comparison between WRF-Chem simulated aerosol profiles with CALIOP data, our emission correction method at Aqua gap and large VZA regions shows robustness in increasing the model simulation accuracy.

# Chapter 6 Conclusion

We developed a correction algorithm for improving emission inventory by using MODIS satellite observations. The approach was applied to the customized FEER 1 km emission data. Our initial analysis indicates that biases in these data caused by three satellite fire detection limitations are from (a) the cloud cover; (b) the insensitivity of fire detection at off-nadir; and (c) the gaps in MODIS swaths at the ground in low latitude regions. These biases are corrected in our study to generate a new spatially continuous emission inventory.

The old and new inventories were applied to WRF-Chem model to simulate smoke loading in the atmosphere. The case study was conducted over NSSA in the high fire month, January 2010. The comparison with MODIS AOD revealed that the new emission lead to an overall improvement in WRF-Chem simulated spatial and temporal distribution of AOD in the study region. Both the daily and monthly mean simulation values are evaluated in our study. When we conducted the emission correction, the emission amount was increased due to filled emission values in regions with cloud cover, large satellite scan angle, and swath gaps. The effect of emission correction method for improving model performance was also confirmed by another model simulation using "scale old" emission. The "scale old" emission has increased old emission amounts measured using the daily ratio of the new and old emissions. The daily and monthly comparison shows that just increasing emission amount is not enough to reduce satellite

fire detection biases. Though there is improvement in standard deviation when comparing "scale old" results with MODIS, there is no enhancement of the correlation between model simulated results and satellite AOD retrievals. The model improvement from the emission correction is also apparent by comparing night time CALIOP-derived AOD at 532 nm with model simulated vertical aerosol loading along CALIPSO track when CALIPSO overpasses the same day's Aqua large VZA or gap regions.

Reducing uncertainties of biomass burning emission is crucial to the reliability of model simulations of atmospheric aerosol physical properties (Zhang et al. 2014). The case study here only presents a simple approach in improving the emission that has inherent limitations from polar-orbiting satellite-based fire detection algorithm in characterizing fires in cloudy conditions and at the edge of or gap areas between satellite ground swath.

# References


Ackerman, S. A., K. I. Strabala, W. P. Menzel, R. A. Frey, C. C. Moeller, and L. E. Gumley, 1998: Discriminating clear sky from clouds with MODIS. *Journal of Geophysical Research: Atmospheres (1984–2012)*, **103,** 32141-32157.

Ackermann, I. J., H. Hass, M. Memmesheimer, A. Ebel, F. S. Binkowski, and U. Shankar, 1998: Modal aerosol dynamics model for Europe: Development and first applications. *Atmospheric environment*, **32,** 2981-2999.

Andreae, M., and Coauthors, 1998: Airborne studies of aerosol emissions from savanna fires in southern Africa: 2. Aerosol chemical composition. *Journal of Geophysical Research: Atmospheres (1984–2012)*, **103,** 32119-32128.

Andreae, M. O., 1991: Biomass burning: its history, use, and distribution and its impact on environmental quality and global climate. *Global biomass burning: Atmospheric, climatic and biospheric implications***,** 3-21.

Andreae, M. O., and P. Merlet, 2001: Emission of trace gases and aerosols from biomass burning. *Global biogeochemical cycles*, **15,** 955-966.

Andreae, M. O., and Coauthors, 1988: Biomass-burning emissions and associated haze layers over Amazonia. *Journal of Geophysical Research: Atmospheres*, **93,** 1509-1527.

Barbosa, P. M., D. Stroppiana, J.-M. Grégoire, and J. C. Pereira, 1999: An assessment of vegetation fire in Africa (1981–1991): Burned areas, burned biomass, and atmospheric emissions. *Global Biogeochemical Cycles*, **13,** 933-950.

Bird, M., and J. Cali, 1998: A million-year record of fire in sub-Saharan Africa. *Nature*, **394,** 767-769.

Boubel, R. W., E. F. Darley, and E. A. Schuck, 1969: Emissions from burning grass stubble and straw. *Journal of the Air Pollution Control Association*, **19,** 497-500.

Bowman, D. M., and Coauthors, 2009: Fire in the Earth system. *science*, **324,** 481-484.

Brass, J. A., L. S. Guild, P. J. Riggan, V. G. Ambrosia, R. N. Lockwood, and A. P. H. Joao, 1996: Characterizing Brazilian fire and estimating areas burned by using the Airborne Infrared Disaster Assessment System. *Biomass Burning and Global Change*, MIT Press, Cambridge, Massachusetts., 561-568.

Cahoon Jr, D. R., B. J. Stocks, J. S. Levine, W. R. Cofer III, and J. M. Pierson, 1994: Satellite analysis of the severe 1987 forest fires in northern China and southeastern Siberia. *Journal of Geophysical Research*, **99,** 18627-18638.

Cardoso, M. F., G. C. Hurtt, B. Moore, C. A. Nobre, and E. M. Prins, 2003: Projecting future fire activity in Amazonia. *Global Change Biology*, **9,** 656-669.

Chen, F., and J. Dudhia, 2001: Coupling an advanced land surface-hydrology model with the Penn State-NCAR MM5 modeling system. Part I: Model implementation and sensitivity. *Monthly Weather Review*, **129,** 569-585.

Chou, M.-D., M. J. Suarez, C.-H. Ho, M. M. Yan, and K.-T. Lee, 1998: Parameterizations for cloud overlapping and shortwave single-scattering properties for use in general circulation and cloud ensemble models. *Journal of climate*, **11,** 202-214.

Christian, T. J., and Coauthors, 2003: Comprehensive laboratory measurements of biomass‐burning emissions: 1. Emissions from Indonesian, African, and other fuels. *Journal of Geophysical Research: Atmospheres*, **108**.

Christopher, S. A., M. Wang, T. A. Berendes, R. M. Welch, and S.-K. Yang, 1998: The 1985 biomass burning season in South America: Satellite remote sensing of fires, smoke, and regional radiative energy budgets. *Journal of Applied Meteorology*, **37,** 661-678.

Crutzen, P. J., and M. O. Andreae, 1990: Biomass burning in the tropics: impact on atmospheric chemistry and biogeochemical cycles. *Science*, **250,** 1669-1678.

Crutzen, P. J., L. E. Heidt, J. P. Krasnec, W. H. Pollock, and W. Seiler, 1979: Biomass burning as a source of atmospheric gases CO, H2, N2O, NO, CH3Cl and COS. *Nature*, **282,** 253-256.

Darley, E. F., F. Burleson, E. Mateer, J. T. Middleton, and V. Osterli, 1966: Contribution of burning of agricultural wastes to photochemical air pollution. *Journal of the Air Pollution Control Association*, **16,** 685-690.

Darmenov, A., and A. da Silva, 2013: The quick fire emissions dataset (QFED)–documentation of versions 2.1, 2.2 and 2.4. *NASA Technical Report Series on Global Modeling and Data Assimilation, NASA TM-2013-104606*, **32,** 183.

Detwiler, R., C. A. Hall, and P. Bogdonoff, 1985: Land use change and carbon exchange in the tropics: II. Estimates for the entire region. *Environmental Management*, **9,** 335-344.

Dozier, J., 1981: A method for satellite identification of surface temperature fields of subpixel resolution. *Remote Sensing of environment*, **11,** 221-229.

Dubovik, O., A. Smirnov, B. Holben, M. King, Y. Kaufman, T. Eck, and I. Slutsker, 2000: Accuracy assessments of aerosol optical properties retrieved from Aerosol Robotic Network(AERONET) Sun and sky radiance measurements. *Journal of Geophysical Research*, **105,** 9791-9806.

Dwyer, E., S. Pinnock, J.-M. Grégoire, and J. Pereira, 2000: Global spatial and temporal distribution of vegetation fire as determined from satellite observations. *International Journal of Remote Sensing*, **21,** 1289-1302.

Eck, T., and Coauthors, 1999: Wavelength dependence of the optical depth of biomass burning, urban, and desert dust aerosols. *J Geophys Res*, **104,** 00093-00095.

Fast, J. D., and Coauthors, 2006: Evolution of ozone, particulates, and aerosol direct radiative forcing in the vicinity of Houston using a fully coupled meteorology‐chemistry‐aerosol model. *Journal of Geophysical Research: Atmospheres (1984–2012)*, **111**.

Flannigan, M. D., and T. V. Haar, 1986: Forest fire monitoring using NOAA satellite AVHRR. *Canadian Journal of Forest Research*, **16,** 975-982.

Freeborn, P. H., M. J. Wooster, and G. Roberts, 2011: Addressing the spatiotemporal sampling design of MODIS to provide estimates of the fire radiative energy emitted from Africa. *Remote Sensing of Environment*, **115,** 475-489.

Gerstle, R., and D. Kemnitz, 1967: Atmospheric emissions from open burning. *Journal of the Air Pollution Control Association*, **17,** 324-327.

Giglio, L., 2007: Characterization of the tropical diurnal fire cycle using VIRS and MODIS observations. *Remote Sensing of Environment*, **108,** 407-421.

Giglio, L., 2010: MODIS collection 5 active fire product user's guide version 2.4.

Giglio, L., J. Kendall, and R. Mack, 2003: A multi-year active fire dataset for the tropics derived from the TRMM VIRS. *International Journal of Remote Sensing*, **24,** 4505-4525.

Giglio, L., I. Csiszar, and C. O. Justice, 2006a: Global distribution and seasonality of active fires as observed with the Terra and Aqua Moderate Resolution Imaging Spectroradiometer (MODIS) sensors. *Journal of Geophysical Research: Biogeosciences*, **111**.

Giglio, L., W. Schroeder, and C. O. Justice, 2016: The collection 6 MODIS active fire detection algorithm and fire products. *Remote Sensing of Environment*, **178,** 31-41.

Giglio, L., G. Van der Werf, J. Randerson, G. Collatz, and P. Kasibhatla, 2006b: Global estimation of burned area using MODIS active fire observations. *Atmospheric Chemistry and Physics*, **6,** 957-974.

Giglio, L., T. Loboda, D. P. Roy, B. Quayle, and C. O. Justice, 2009: An active-fire based burned area mapping algorithm for the MODIS sensor. *Remote Sensing of Environment*, **113,** 408-420.

Giglio, L., J. Randerson, G. Van der Werf, P. Kasibhatla, G. Collatz, D. Morton, and R. DeFries, 2010: Assessing variability and long-term trends in burned area by merging multiple satellite fire products. *Biogeosciences,* **7**.

Grell, G., S. Freitas, M. Stuefer, and J. Fast, 2011: Inclusion of biomass burning in WRF-Chem: impact of wildfires on weather forecasts. *Atmos. Chem. Phys*, **11,** 5289-5303.

Grell, G. A., and D. Dévényi, 2002: A generalized approach to parameterizing convection combining ensemble and data assimilation techniques. *Geophysical Research Letters*, **29,** 38-31-38-34.

Grell, G. A., S. E. Peckham, R. Schmitz, S. A. McKeen, G. Frost, W. C. Skamarock, and B. Eder, 2005: Fully coupled "online" chemistry within the WRF model. *Atmospheric Environment*, **39,** 6957-6975.

Hao, W. M., and M.-H. Liu, 1994: Spatial and temporal distribution of tropical biomass burning. *Global biogeochemical cycles,* **8,** 495-503.

Hao, W. M., M.-H. Liu, and P. J. Crutzen, 1990: Estimates of annual and regional releases of CO2 and other trace gases to the atmosphere from fires in the tropics, based on the FAO statistics for the period 1975–1980. *Fire in the tropical biota,* Springer, 440-462.

Heald, C. L., D. J. Jacob, P. I. Palmer, M. J. Evans, G. W. Sachse, H. B. Singh, and D. R. Blake, 2003: Biomass burning emission inventory with daily resolution: Application to aircraft observations of Asian outflow. *Journal of Geophysical Research: Atmospheres*, **108**.

Hoelzemann, J. J., M. G. Schultz, G. P. Brasseur, C. Granier, and M. Simon, 2004: Global Wildland Fire Emission Model (GWEM): Evaluating the use of global area burnt satellite data. *Journal of Geophysical Research: Atmospheres*, **109**.

Hoffa, E. A., D. Ward, W. Hao, R. Susott, and R. Wakimoto, 1999: Seasonality of carbon emissions from biomass burning in a Zambian savanna. *Journal of Geophysical Research: Atmospheres*, **104,** 13841-13853.

Holben, B., and Coauthors, 1998: AERONET—A federated instrument network and data archive for aerosol characterization. *Remote sensing of environment*, **66,** 1-16.

Hong, S.-Y., Y. Noh, and J. Dudhia, 2006: A new vertical diffusion package with an explicit treatment of entrainment processes. *Monthly Weather Review*, **134,** 2318-2341.

Houghton, R. A., and Coauthors, 1985: Net flux of carbon dioxide from tropical forests in 1980. *Nature*, **316,** 617-620.

Hyer, E., J. Reid, and J. Zhang, 2011: An over-land aerosol optical depth data set for data assimilation by filtering, correction, and aggregation of MODIS Collection 5 optical depth retrievals. *Atmospheric Measurement Techniques*, **4,** 379-408.

Hyer, E., J. Wang, and A. Arellano, 2012: Biomass burning: observations, modeling, and data assimilation. *Bulletin of the American Meteorological Society*, **93,** ES10.

Ichoku, C., and Y. J. Kaufman, 2005: A method to derive smoke emission rates from MODIS fire radiative energy measurements. *Geoscience and Remote Sensing, IEEE Transactions on*, **43,** 2636-2649.

Ichoku, C., and L. Ellison, 2014: Global top-down smoke-aerosol emissions estimation using satellite fire radiative power measurements. *Atmospheric Chemistry and Physics*, **14,** 6643-6667.

Ichoku, C., R. Kahn, and M. Chin, 2012: Satellite contributions to the quantitative characterization of biomass burning for climate modeling. *Atmospheric Research*, **111,** 1-28.

Ichoku, C., L. Giglio, M. J. Wooster, and L. A. Remer, 2008: Global characterization of biomass-burning patterns using satellite measurements of fire radiative energy. *Remote Sensing of Environment*, **112,** 2950-2962.

Ichoku, C., and Coauthors, 2002: A spatio-temporal approach for global validation and analysis of MODIS aerosol products. *Geophysical Research Letters*, **29,** MOD 1-1–MOD 1-4.

Ito, A., and J. E. Penner, 2004: Global estimates of biomass burning emissions based on satellite imagery for the year 2000. *Journal of Geophysical Research: Atmospheres*, **109**.

Justice, C., and Coauthors, 2002: The MODIS fire products. *Remote Sensing of Environment*, **83,** 244-262.

Kaiser, J., and Coauthors, 2012: Biomass burning emissions estimated with a global fire assimilation system based on observed fire radiative power. *Biogeosciences*, **9,** 527-554.

Kalnay, E., and Coauthors, 1996: The NCEP/NCAR 40-year reanalysis project. *Bulletin of the American meteorological Society*, **77,** 437-471.

Kaufman, Y. J., and Coauthors, 1998: Potential global fire monitoring from EOS-MODIS. *Journal of Geophysical Research: Atmospheres*, **103,** 32215-32238.

Levine, J. S., 1991: *Global biomass burning: atmospheric, climatic, and biospheric implications.* MIT press.

Levy, R., S. Mattoo, L. Munchak, L. Remer, A. Sayer, and N. Hsu, 2013: The Collection 6 MODIS aerosol products over land and ocean. *Atmos. Meas. Tech*, **6,** 2989-3034.

Levy, R. C., L. A. Remer, and O. Dubovik, 2007: Global aerosol optical properties and application to Moderate Resolution Imaging Spectroradiometer aerosol retrieval over land. *Journal of Geophysical Research: Atmospheres (1984–2012)*, **112**.

Levy, R. C., L. A. Remer, R. G. Kleidman, S. Mattoo, C. Ichoku, R. Kahn, and T. Eck, 2010: Global evaluation of the Collection 5 MODIS dark-target aerosol products over land. *Atmospheric Chemistry and Physics*, **10,** 10399-10420.

Lighty, J. S., J. M. Veranth, and A. F. Sarofim, 2000: Combustion aerosols: factors governing their size and composition and implications to human health. *Journal of the Air & Waste Management Association*, **50,** 1565-1618.

Lin, Y.-L., R. D. Farley, and H. D. Orville, 1983: Bulk parameterization of the snow field in a cloud model. *Journal of Climate and Applied Meteorology*, **22,** 1065-1092.

Mlawer, E. J., S. J. Taubman, P. D. Brown, M. J. Iacono, and S. A. Clough, 1997: Radiative transfer for inhomogeneous atmospheres: RRTM, a validated correlated-k model for the longwave. *Journal of Geophysical Research: Atmospheres (1984–2012)*, **102,** 16663-16682.

Mouillot, F., M. G. Schultz, C. Yue, P. Cadule, K. Tansey, P. Ciais, and E. Chuvieco, 2014: Ten years of global burned area products from spaceborne remote sensing—A review: Analysis of user needs and recommendations for future developments. *International Journal of Applied Earth Observation and Geoinformation*, **26,** 64-79.

Mu, M., and Coauthors, 2011: Daily and 3-hourly variability in global fire emissions and consequences for atmospheric model predictions of carbon monoxide. *Journal of Geophysical Research: Atmospheres*, **116**.

Polivka, T. N., 2015: Improving Nocturnal Fire Detection with the VIIRS Day-Night Band. M.S., Dept. of Earth and Atmospheric Sciences, University of Nebraks-Lincoln, 76 pp.

Power, M. J., and Coauthors, 2008: Changes in fire regimes since the Last Glacial Maximum: an assessment based on a global synthesis and analysis of charcoal data. *Climate dynamics*, **30,** 887-907.

Prins, E. M., and W. Menzel, 1992: Geostationary satellite detection of bio mass burning in South America. *International Journal of Remote Sensing*, **13,** 2783-2799.

Prins, E. M., and W. P. Menzel, 1994: Trends in South American biomass burning detected with the GOES visible infrared spin scan radiometer atmospheric sounder from 1983 to 1991. *Journal of Geophysical Research: Atmospheres*, **99,** 16719-16735.

Ramanathan, V., R. J. Cicerone, H. B. Singh, and J. T. Kiehl, 1985: Trace gas trends and their potential role in climate change. *Journal of Geophysical Research: Atmospheres*, **90,** 5547-5566.

Reid, J., R. Koppmann, T. Eck, and D. Eleuterio, 2005: A review of biomass burning emissions part II: intensive physical properties of biomass burning particles. *Atmospheric Chemistry and Physics*, **5,** 799-825.

Reid, J. S., and Coauthors, 2004: Real-time monitoring of South American smoke particle emissions and transport using a coupled remote sensing/box-model approach. *Geophysical Research Letters*, **31**.

Reid, J. S., and Coauthors, 2009: Global monitoring and forecasting of biomass-burning smoke: Description of and lessons from the Fire Locating and Modeling of Burning Emissions (FLAMBE) program. *Selected Topics in Applied Earth Observations and Remote Sensing, IEEE Journal of*, **2,** 144-162.

Remer, L. A., and Coauthors, 2005: The MODIS aerosol algorithm, products, and validation. *Journal of the atmospheric sciences*, **62,** 947-973.

Remer, L. A., and Coauthors, 2008: Global aerosol climatology from the MODIS satellite sensors. *Journal of Geophysical Research: Atmospheres*, **113**.

Roberts, G., M. Wooster, and E. Lagoudakis, 2009: Annual and diurnal african biomass burning temporal dynamics. *Biogeosciences*, **6**.

Roberts, G., M. J. Wooster, G. L. Perry, N. Drake, L. M. Rebelo, and F. Dipotso, 2005: Retrieval of biomass combustion rates and totals from fire radiative power observations: Application to southern Africa using geostationary SEVIRI imagery. *Journal of Geophysical Research: Atmospheres*, **110**.

Roberts, G. J., and M. J. Wooster, 2008: Fire detection and fire characterization over Africa using Meteosat SEVIRI. *Geoscience and Remote Sensing, IEEE Transactions on*, **46,** 1200-1218.

Robinson, J. M., 1991: Fire from space: Global fire evaluation using infrared remote sensing. *International Journal of Remote Sensing*, **12,** 3-24.

Roy, D., P. Lewis, and C. Justice, 2002: Burned area mapping using multi-temporal moderate spatial resolution data—A bi-directional reflectance model-based expectation approach. *Remote Sensing of Environment*, **83,** 263-286.

Saide, P. E., and Coauthors, 2015: Revealing important nocturnal and day-to-day variations in fire smoke emissions through a multiplatform inversion. *Geophysical Research Letters*, **42,** 3609-3618.

Sandberg, D., S. Pickford, and E. Darley, 1975: Emissions from slash burning and the influence of flame retardant chemicals. *Journal of the Air Pollution Control Association*, **25,** 278-281.

Sayer, A., N. Hsu, C. Bettenhausen, and M. J. Jeong, 2013: Validation and uncertainty estimates for MODIS Collection 6 "Deep Blue" aerosol data. *Journal of Geophysical Research: Atmospheres*, **118,** 7864-7872.

Schell, B., I. J. Ackermann, H. Hass, F. S. Binkowski, and A. Ebel, 2001: Modeling the formation of secondary organic aerosol within a comprehensive air quality model system. *Journal of Geophysical Research: Atmospheres (1984–2012)*, **106,** 28275-28293.

Schroeder, W., I. Csiszar, and J. Morisette, 2008: Quantifying the impact of cloud obscuration on remote sensing of active fires in the Brazilian Amazon. *Remote Sensing of Environment*, **112,** 456-470.

Schüle, W., 1990: Landscapes and climate in prehistory: interactions of wildlife, man, and fire. *Fire in the tropical biota*, Springer, 273-318.

Scott, A. C., and I. J. Glasspool, 2006: The diversification of Paleozoic fire systems and fluctuations in atmospheric oxygen concentration. *Proceedings of the National Academy of Sciences*, **103,** 10861-10865.

Seiler, W., and P. J. Crutzen, 1980: Estimates of gross and net fluxes of carbon between the biosphere and the atmosphere from biomass burning. *Climatic change*, **2,** 207-247.

Shea, R. W., B. W. Shea, J. B. Kauffman, D. E. Ward, C. I. Haskins, and M. C. Scholes, 1996: Fuel biomass and combustion factors associated with fires in savanna ecosystems of South Africa and Zambia. *Journal of Geophysical Research: Atmospheres*, **101,** 23551-23568.

Shi, Y., T. Matsunaga, and Y. Yamaguchi, 2015: High-Resolution Mapping of Biomass Burning Emissions in Three Tropical Regions. *Environmental science & technology*, **49,** 10806-10814.

Shi, Y., J. Zhang, J. Reid, E. Hyer, and N. Hsu, 2013: Critical evaluation of the MODIS Deep Blue aerosol optical depth product for data assimilation over North Africa. *Atmos. Meas. Tech*, **6,** 949-969.

Simon, M., S. Plummer, F. Fierens, J. J. Hoelzemann, and O. Arino, 2004: Burnt area detection at global scale using ATSR-2: The GLOBSCAR products and their qualification. *Journal of Geophysical Research: Atmospheres*, **109**.

Stockwell, W. R., P. Middleton, J. S. Chang, and X. Tang, 1990: The second generation regional acid deposition model chemical mechanism for regional air quality modeling. *Journal of Geophysical Research: Atmospheres (1984–2012)*, **95,** 16343-16367.

Tansey, K., and Coauthors, 2004: Vegetation burning in the year 2000: Global burned area estimates from SPOT VEGETATION data. *Journal of Geophysical Research: Atmospheres*, **109**.

Theisen, M., E. Prins, C. Schmidt, J. Reid, J. Hunter, and D. Westphal, 2002: Data filtering of Western Hemisphere GOES wildfire ABBA products. *AGU Spring Meeting Abstracts*.

Tosca, M., D. Diner, M. Garay, and O. Kalashnikova, 2014: Observational evidence of fire-driven reduction of cloud fraction in tropical Africa. *Journal of Geophysical Research: Atmospheres*, **119,** 8418-8432.

van der Werf, G. R., J. T. Randerson, L. Giglio, G. J. Collatz, P. S. Kasibhatla, and A. F. Arellano Jr, 2006: Interannual variability in global biomass burning emissions from 1997 to 2004. *Atmospheric Chemistry and Physics*, **6,** 3423-3441.

van der Werf, G. R., and Coauthors, 2010: Global fire emissions and the contribution of deforestation, savanna, forest, agricultural, and peat fires (1997–2009). *Atmospheric Chemistry and Physics*, **10,** 11707-11735.

Van Leeuwen, T., and G. Van Der Werf, 2011: Spatial and temporal variability in the ratio of trace gases emitted from biomass burning. *Atmospheric Chemistry and Physics*, **11,** 3611-3629.

Vermote, E., and D. Roy, 2002: Land surface hot-spot observed by MODIS over Central Africa. *International Journal of Remote Sensing*, **23,** 2141-2143.

Wang, J., S. A. Christopher, U. Nair, J. S. Reid, E. M. Prins, J. Szykman, and J. L. Hand, 2006: Mesoscale modeling of Central American smoke transport to the United States: 1."Top-down" assessment of emission strength and diurnal variation impacts. *Journal of Geophysical Research: Atmospheres (1984–2012)*, **111**.

Watson, C. E., J. Fishman, and H. G. Reichle, 1990: The significance of biomass burning as a source of carbon monoxide and ozone in the southern hemisphere tropics: A satellite analysis. *Journal of Geophysical Research: Atmospheres*, **95,** 16443-16450.

Wiedinmyer, C., S. Akagi, R. J. Yokelson, L. Emmons, J. Al-Saadi, J. Orlando, and A. Soja, 2011: The Fire INventory from NCAR (FINN): A high resolution global model to estimate the emissions from open burning. *Geoscientific Model Development*, **4,** 625.

Wolfe, R. E., M. Nishihama, A. J. Fleig, J. A. Kuyper, D. P. Roy, J. C. Storey, and F. S. Patt, 2002: Achieving sub-pixel geolocation accuracy in support of MODIS land science. *Remote Sensing of Environment*, **83,** 31-49.

Wooster, M. J., 2002: Small-scale experimental testing of fire radiative energy for quantifying mass combusted in natural vegetation fires. *Geophysical Research Letters*, **29**.

Yang, Z., J. Wang, C. Ichoku, E. Hyer, and J. Zeng, 2013: Mesoscale modeling and satellite observation of transport and mixing of smoke and dust particles over northern sub-Saharan African region. *Journal of Geophysical Research: Atmospheres*, **118,** 12,139-112,157.

Zhang, F., and Coauthors, 2014: Sensitivity of mesoscale modeling of smoke direct radiative effect to the emission inventory: a case study in northern sub-Saharan African region. *Environmental Research Letters*, **9,** 075002.

Zhang, J., and J. S. Reid, 2006: MODIS aerosol product analysis for data assimilation: Assessment of over-ocean level 2 aerosol optical thickness retrievals. *Journal of Geophysical Research: Atmospheres*, **111**.

Zhang, X., and S. Kondragunta, 2008: Temporal and spatial variability in biomass burned areas across the USA derived from the GOES fire product. *Remote Sensing of Environment*, **112,** 2886-2897.

Zhang, X., S. Kondragunta, J. Ram, C. Schmidt, and H. C. Huang, 2012: Near-real-time global biomass burning emissions product from geostationary satellite constellation. *Journal of Geophysical Research: Atmospheres*, **117**.

**Tables**

Table 1. Comparisons of different smoke emission inventories based on bottom-up method using satellite data

| Study | Reid et al. (2004, 2009) FLAMBE | Hoelzemann et al. (2004) | van der Werf et al. (2010) GFED3 | Wiedinmyer et al. (2011) FINN |
|---|---|---|---|---|
| **Parameters** | | | | |
| Land cover map data source | USGS | IGBP and MODIS | MOD12 with UMD | IGBP and MODIS |
| Fuel load ($kg/m^2$) | Compiled fuel load map for specific regional ecosystems | Applying vegetation model LPJ-DGVM | Vegetation model (van der Werf et al. 2006) | Vegetation model (Hoelzemann et al.2004) |
| Burn area ($m^2$) method | Active fire | Burn scare | Burn scar | Active fire |
| EF (g/kg) | Literature survey (J. S. Reid 2005) | Data from Andreae and Merlet (2001) | Data from Andreae and Merlet (2001) | Akagi et al. (2011) and Andreae and Merlet (2001) |
| Combustion completeness (-) | Literature survey (J. S. Reid 2005) | Literature survey J. S. Reid (2005) | Scaled value according to moisture (van der Werf et al. 2006) | Literature survey for different land types (Ito and Penner 2004) |
| **Bias correction** | | | | |
| Swath gap | No | Yes (ATSR fire counts) | Yes (Filled in the newest version GFED4) | Yes (Filled with half size of previous day's) |
| Large VZA | No | No | No | No |
| Cloud cover | No | No | No | No |

Table 2. Comparisons of different smoke emission inventories based on top-down method

| Study | Kaiser et al. (2012) GFASv1.0 | Darmenov and da Silva (2013) QFED | Ichoku and Ellison (2014) FEER.v1 |
|---|---|---|---|
| **Parameters** | | | |
| FRP (W) | MODIS | MODIS | MODIS and Kaiser et al. (2012) |
| Land cover map | Heil et al. (2010, 2012) | IGBP | Rather than using EF and conversion factor, developed $C_e$ |
| EF (g/kg) | Andreae and Merlet (2001) and Christian et al. (2003) | Andreae and Merlet (2001) | |
| $\alpha^*$ (kg/MJ) | Heil et al. (2010, 2012) | Kaiser et al. (2009) | |
| **Bias correction** | | | |
| Swath gap | Yes (Previous day's data) | Yes (same as Kaiser et al. [2012]) | Yes (same as Kaiser et al. [2012]) |
| Large VZA | No | No | No |
| Cloud cover | Yes (Clear sky FRP density stands for whole grid) | Yes (same as Kaiser et al. [2012]) | Yes (same as Kaiser et al. [2012]) |

$\alpha^*$ is a conversion factor that links FRP to dry matter combustion rate.

Table 3. Configuration Options Employed by WRF-Chem in This Study

| Atmospheric Processes | Model Options |
|---|---|
| Shortwave radiation | Goddard |
| Longwave radiation | RRTM |
| Gas-phase mechanism | RADM2 |
| Aerosol model | MADE/SORGAM |
| Land surface model | Noah |
| Boundary layer scheme | YSU |
| Microphysics | Lin et al. |
| Cumulus | New Grell |

Table 4. Filters, thresholds, and data loss in QA for Terra DT (Aqua DT in parentheses)

| | QA flag | SA | Cloud fraction | Buddy |
|---|---|---|---|---|
| Thresholds | "Very Good" | SA<170° | $F_{cld}$ <0% | Isolated retrieval |
| Data loss | 37.21%(42.47%) | 0.23%(0.17%) | 10.35%(10.62%) | 0.37%(0.47%) |

Table 5. Filters, thresholds, and data loss in QA for Terra DB (Aqua DB in parentheses)

| | QA flag | Cloud fraction | Buddy | STE |
|---|---|---|---|---|
| Thresholds | "Very Good" | $F_{cld}$ <60% | Isolated retrieval | STE<0.03 |
| Data loss | 25.73% (30.00%) | 1.50% (1.00%) | 0.13% (0.16%) | 3.41% (3.33%) |

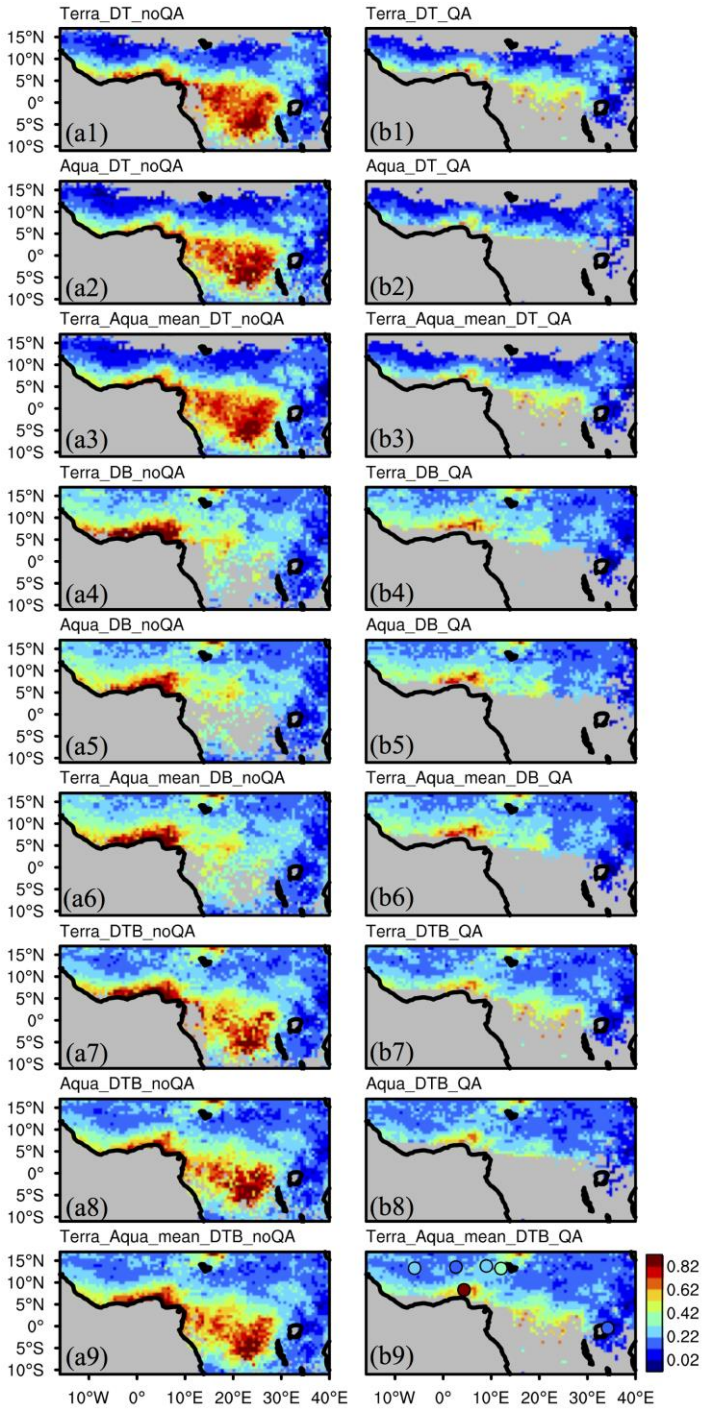


Figure 1. (a1)–(a9): Monthly Terra DT, Aqua DT, Terra Aqua Mean DT, Terra DB, Aqua DB, Terra Aqua DB, Terra DTB, Aqua DTB, and Terra Aqua DTB AOD at 0.55 μm before QA in January 2010. (b1)–(b9) are similar to (a1)–(a9) but for AODs after QA. The filled circles in (b9) indicate AERONET monthly average AOD at 0.55 μm.

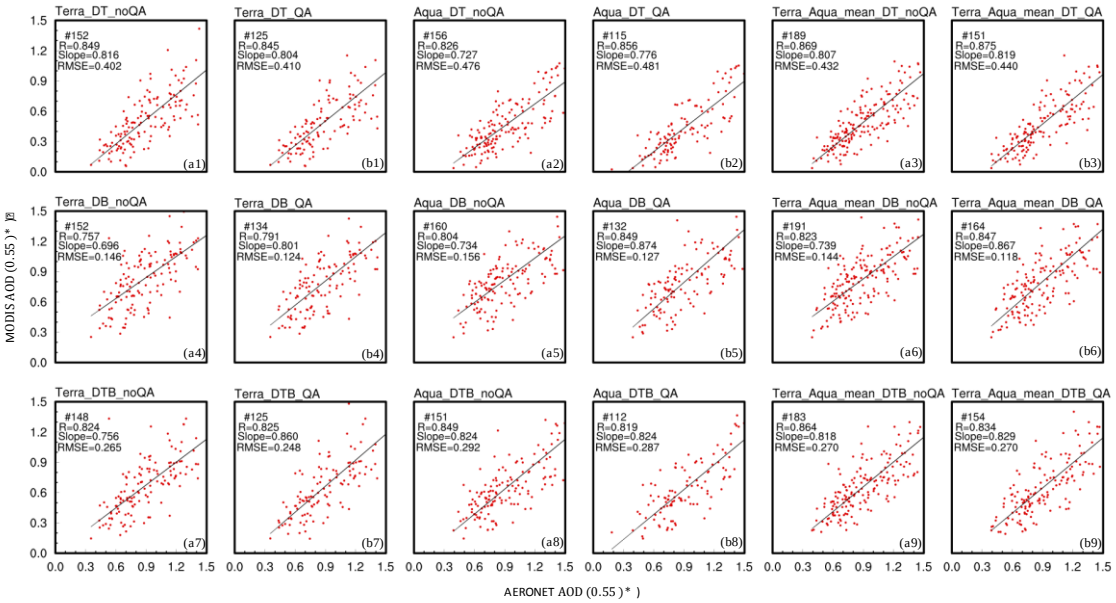


Figure 2. Regional comparisons between daily MODIS AOD and AERONET AOD at 0.55 μm. (a1)–(a9) indicate Terra DT, Aqua DT, Terra Aqua Mean DT, Terra DB, Aqua DB, Terra Aqua DB, Terra DTB, Aqua DTB, and Terra Aqua DTB AOD before QA, (b1)–(b9) are MODIS AOD after QA.

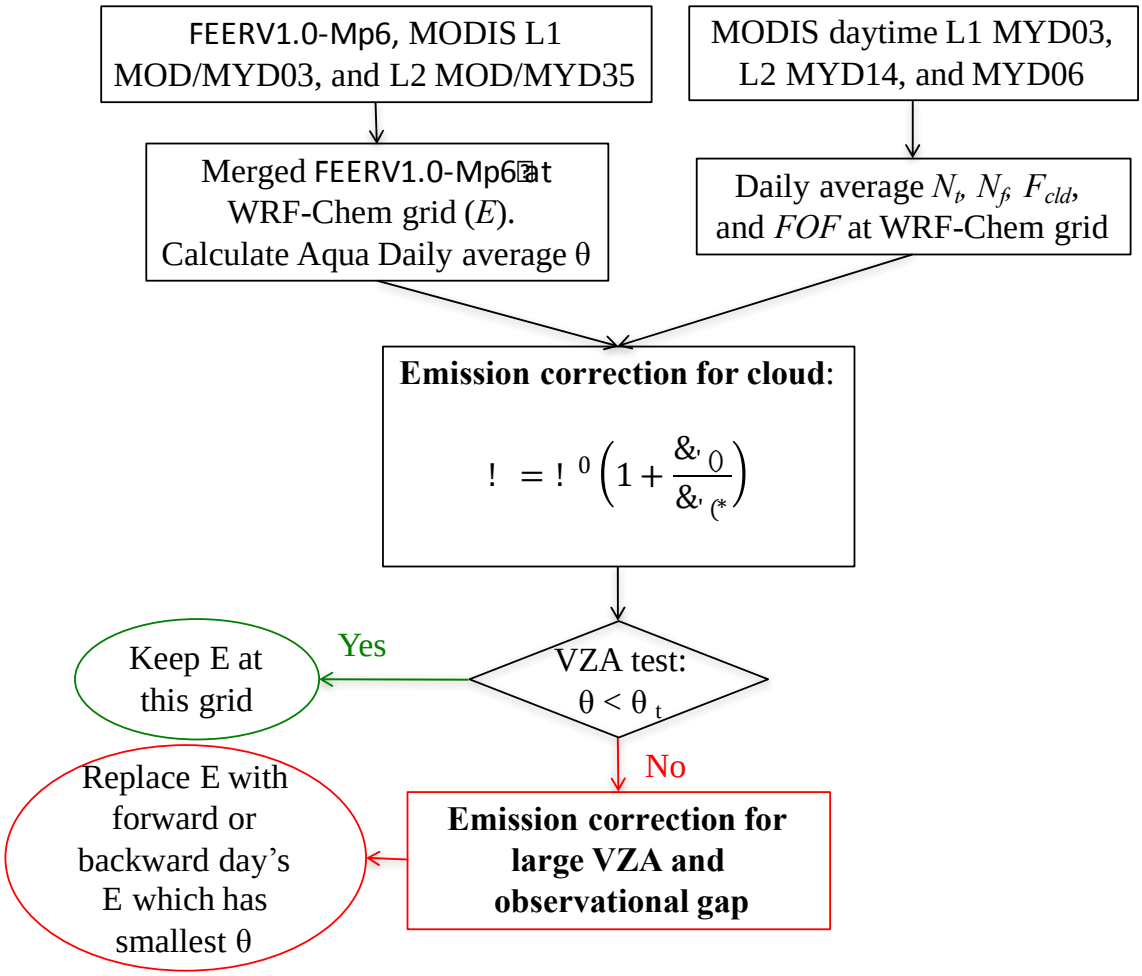


Figure 3. Flowchart of emission bias correction method.

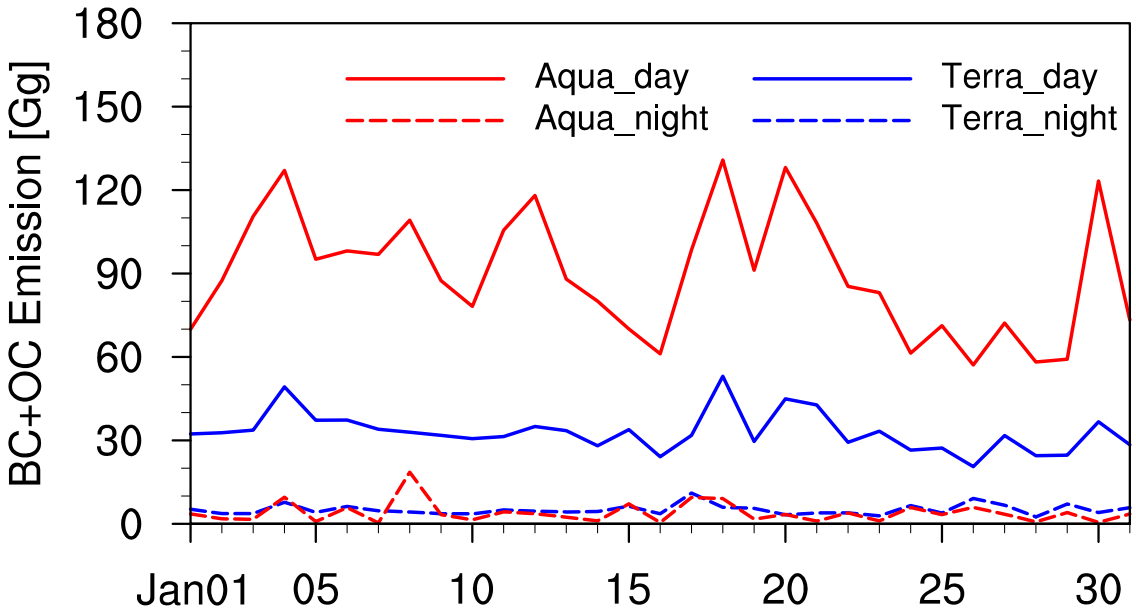


Figure 4. Time series of inner domain total BC+OC emission from different satellites in day and night.

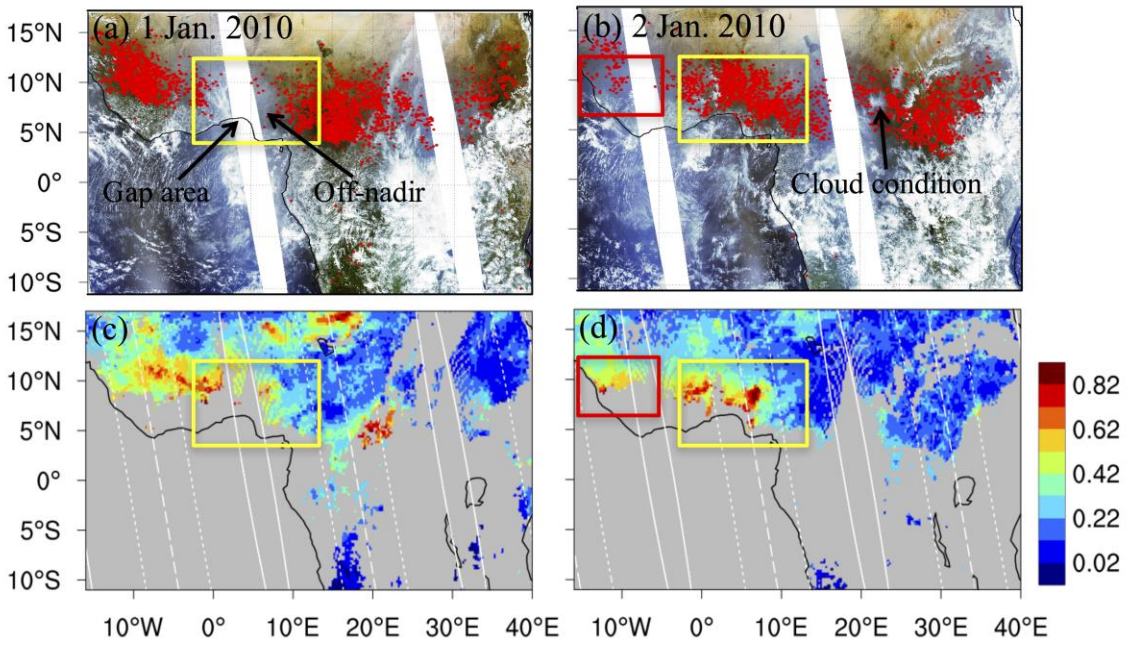


Figure 5. (a)–(b): Aqua MODIS true color image overlaid with daytime fires (red dots) on January 1 and 2, 2010. (c)–(d): MODIS Terra Aqua DB AOD after QA at 0.55 $\mu m$ on the same days of (a-b). (The white solid, dot, and dash lines in (c) and (d) stand for Aqua swath borders, Aqua $\theta$ = 35 ° tracks, and satellite nadir view orbits.)

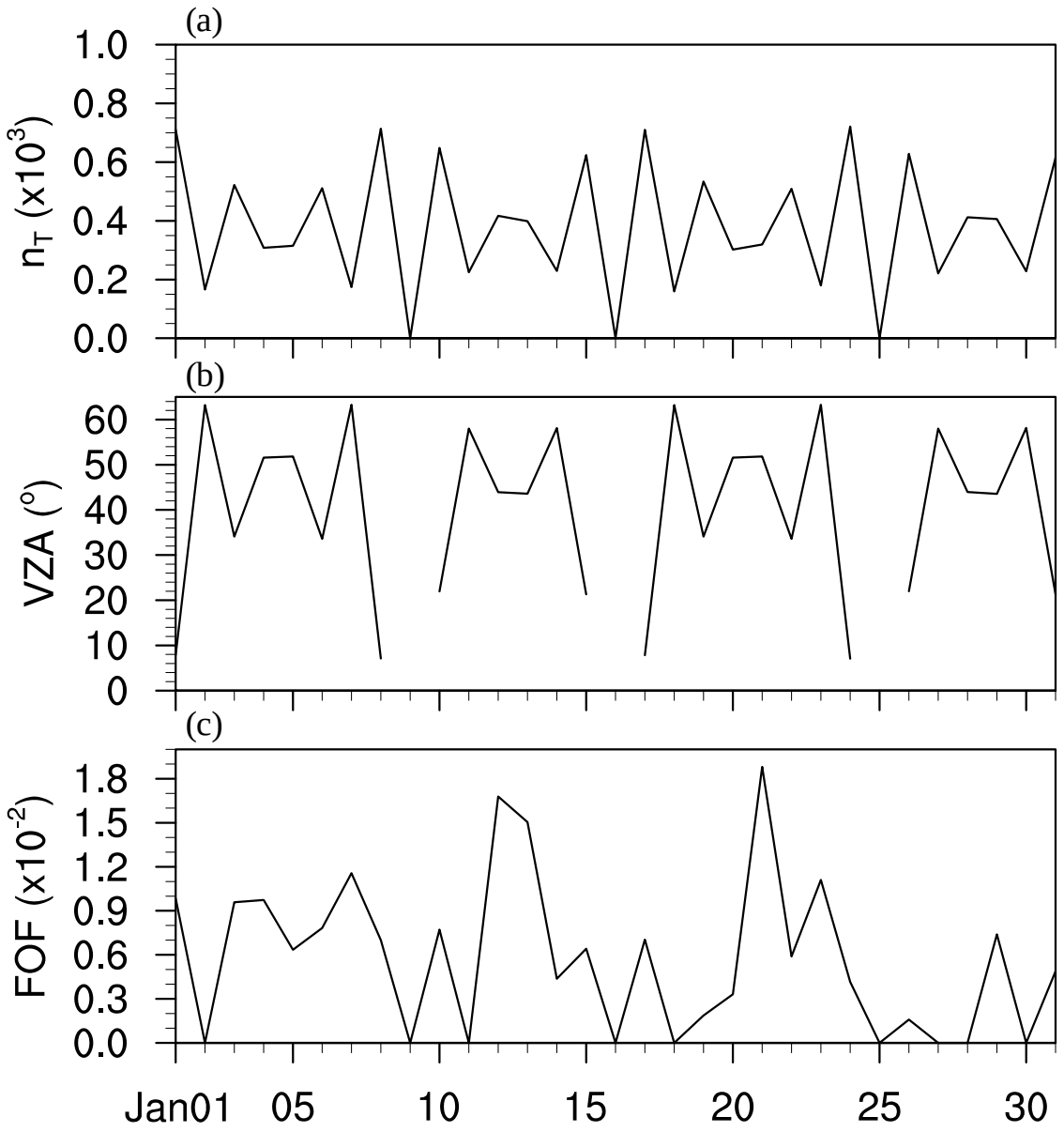


Figure 6. Time series of Aqua gathered total pixel number ($N_t$) (a), daytime averaged View Zenith Angle (VZA) (b), and the Fraction of Fire (FOF) in a model grid at NSSA in 2010 January.

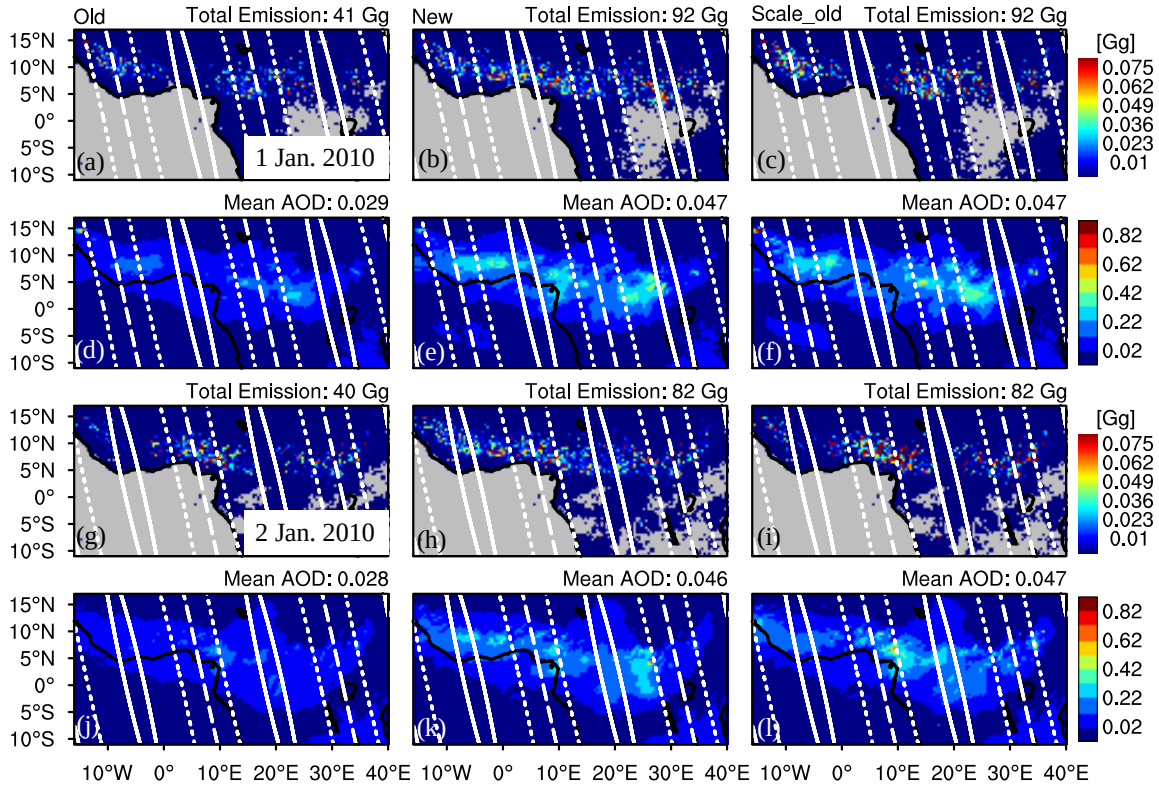


Figure 7. (a)–(c): Old, new, scale old BC+OC emission on January 1st , 2010 at WRF-Chem grid. (d)–(f): WRF-Chem simulated column total AOD at 0.55 μm using the emission of (a)–(c) during Aqua pass period (12:00-14:00 UTC). (g)–(l): Same as (a)–(f) but for January 2nd , 2010. (The white solid, dot, and dash lines stand for Aqua swath borders, Aqua $\theta$ = 35 ° tracks, and satellite nadir view orbits.)

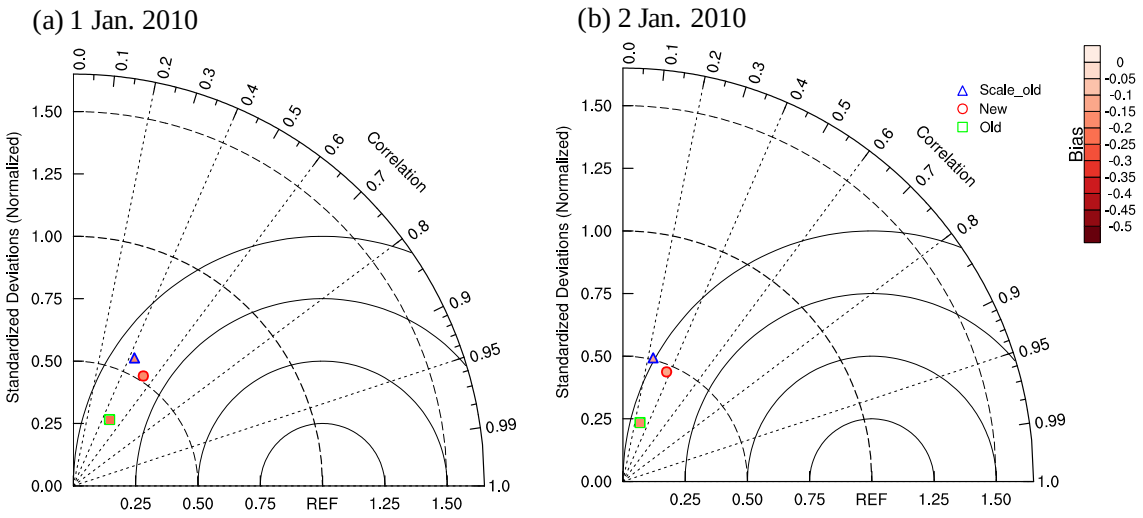


Figure 8. Taylor diagram for WRF-Chem simulated column total AOD at 0.55 µm compared with Terra and Aqua mean DB after QA in January 1st (a) and 2nd (b), 2010 over high smoke loading region. REF is MODIS observation. Different fill colors indicate the biases between model and MODIS.

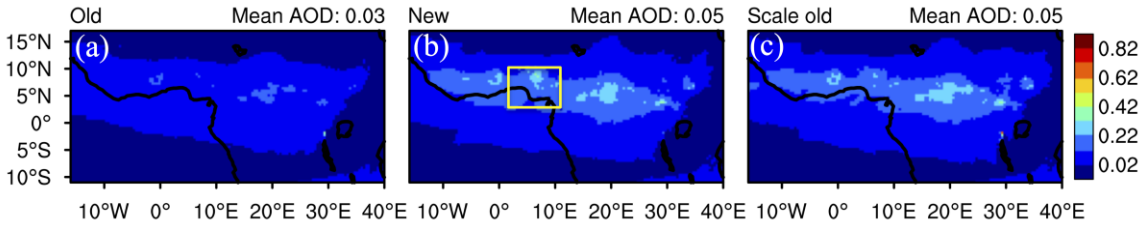


Figure 9. Monthly average WRF-Chem simulated column total AOD at 0.55 μm during daytime (08:00-20:00 UTC) using old (a), new (b), and scale old (c) emissions for January 2010.

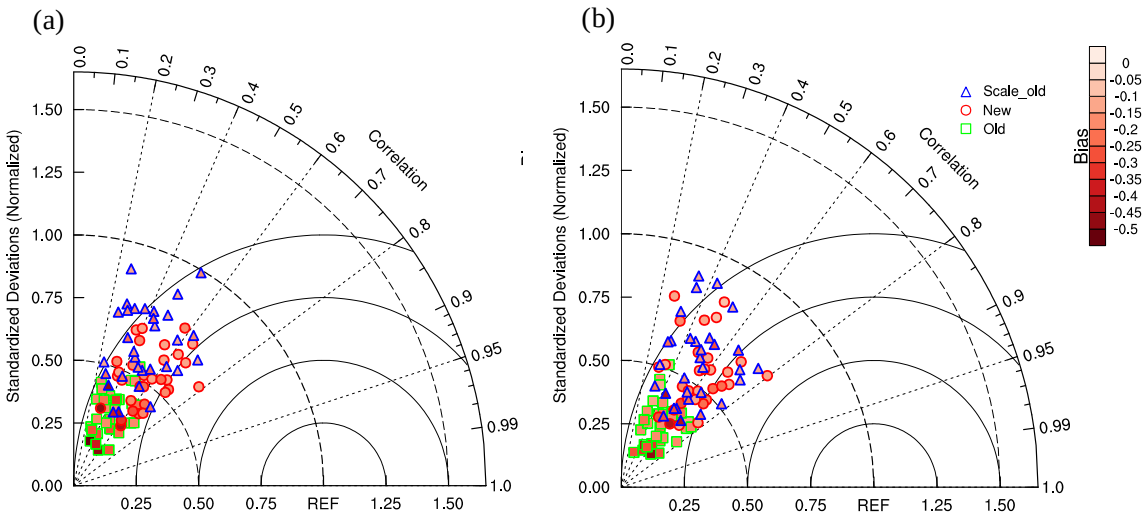


Figure 10. Taylor diagram for WRF-Chem simulated daily column total AOD at 0.55 μm compared with Terra Aqua mean DB after QA within high smoke loading region (a) and WRF-Chem AOD compared with Terra DB AOD after QA at Aqua gap and Aqua $\theta > \theta_t$ over high smoke loading regions (b) in January 2010. REF is MODIS observation. Different fill colors indicate the biases between model and MODIS.

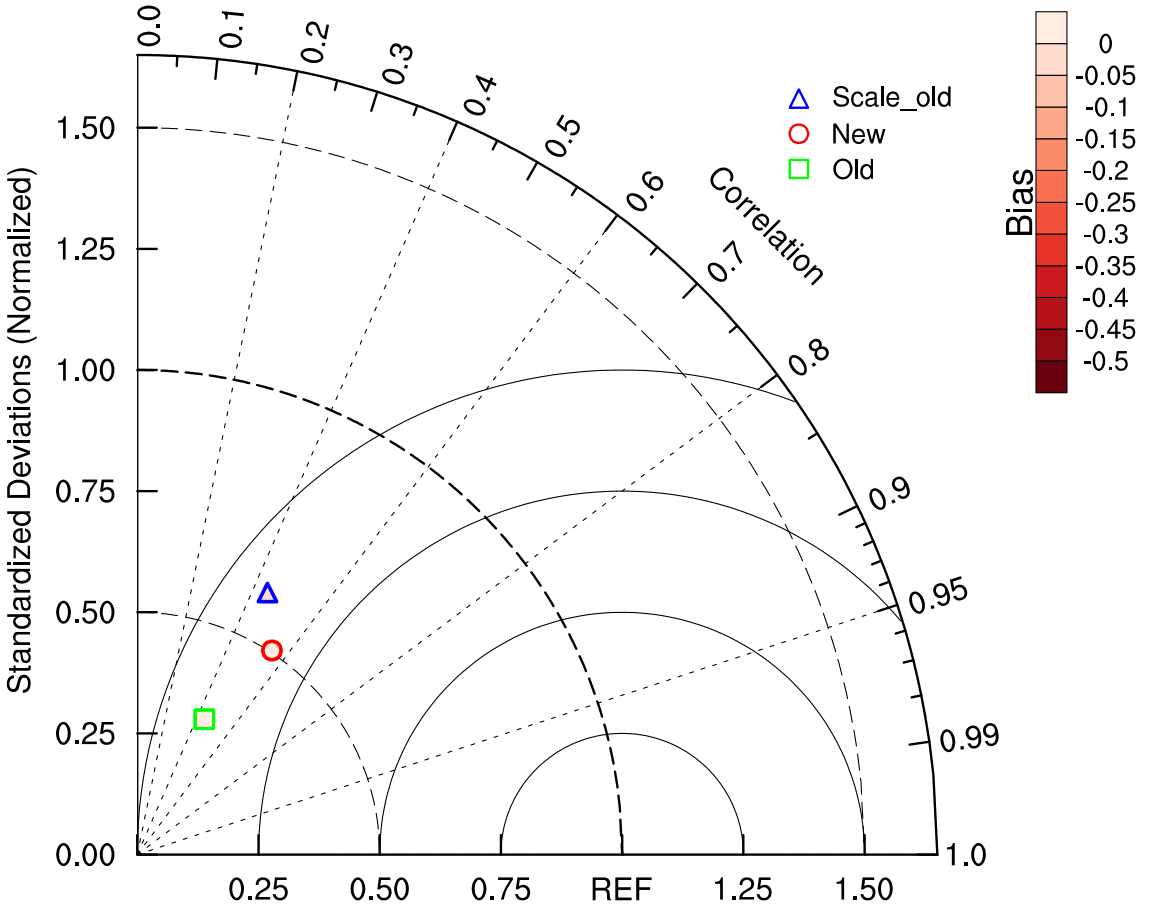


Figure 11. WRF-Chem simulated whole month (January 2010) column total AOD at 0.55 μm AOD compared with Terra DB AOD at Aqua gap and Aqua $\theta > \theta_t$ over high smoke loading region.

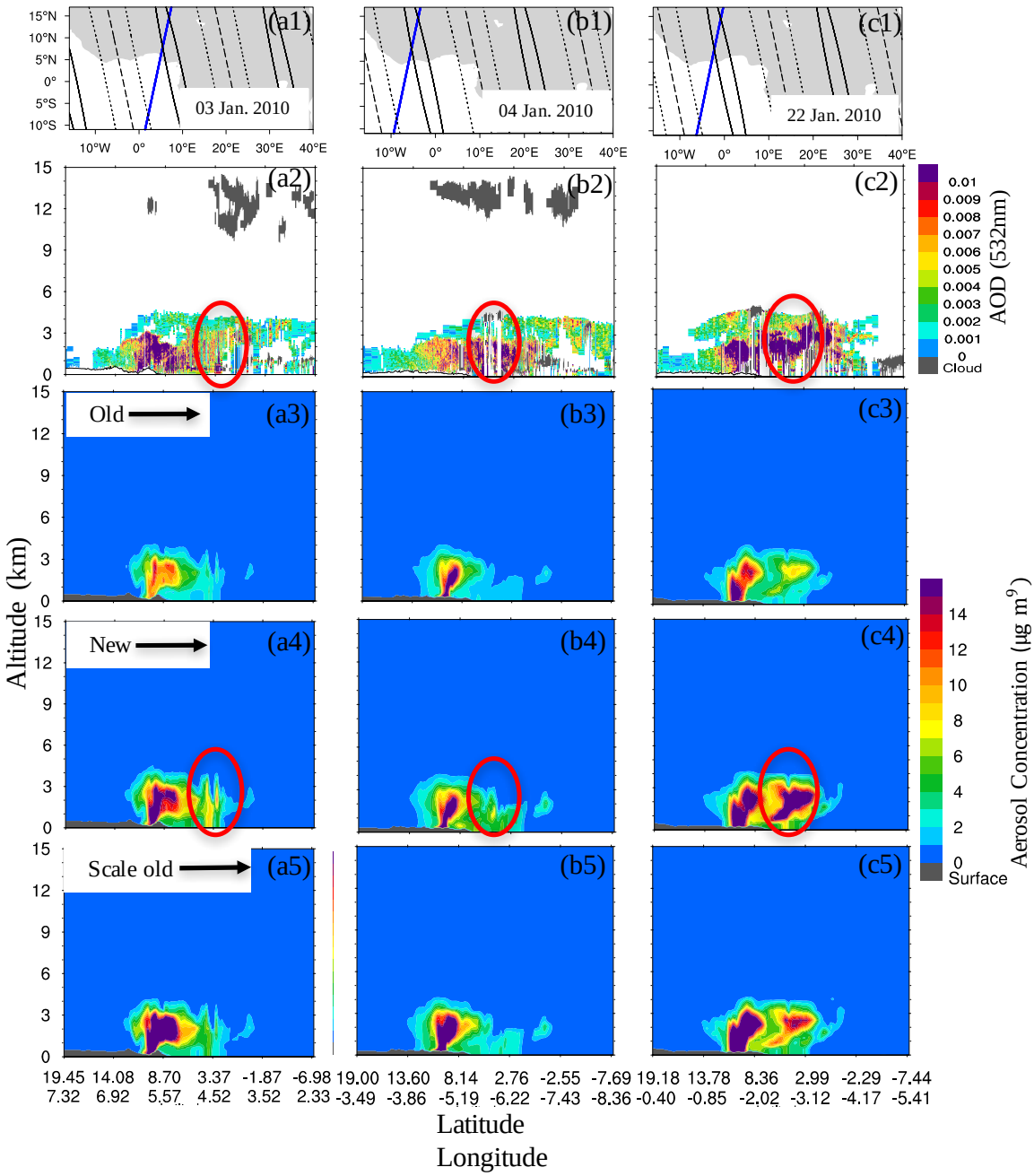


Figure 12. First row shows selected nighttime CALIPSO tracks (blue lines) that pass over day time Aqua large VZA or gap regions (Aqua orbits are also shown in the map and the meaning of different line types are same as Figure 5 (b) and (c).) Comparison of night time CALIOP-derived AOD vertical profile (calculated from aerosol extinction coefficient) at 532 nm (second row), WRF-Chem simulated vertical profiles of smoke concentration along the corresponding CALIPSO ground track using old (third row), new (fourth row), and "scale old" emissions (fifth row). 3, 4, and 22 of January 2010 data are shown from the first column to the third column. Red ovals in second and fourth rows show the CALIOP-derived aerosol loading patterns captured by new model simulations.